STUDY OF TROPICAL DEEP CONVECTIVE PROCESSES AND WATER VAPOR VARIATIONS USING NASA A-TRAIN DATA AND GEOSTATIONARY SATELLITE OBSERVATIONS

by

HANII TAKAHASHI

A dissertation submitted to the Graduate Faculty in Earth and Environmental Science in partial fulfillment of the requirements for the degree of Doctor of Philosophy, The City University of New York

2013

© 2013
HANII TAKAHASHI
All Rights Reserved

This manuscript has been read and accepted for the Graduate Faculty in Earth and Environmental Science in satisfaction of the dissertation requirement for the degree of Doctor of Philosophy.

Dr. Zhengzhao "Johnny" Luo

[required signature]

Date — Chair of Examining Committee

Dr. Cindi Katz

[required signature]

Date — Executive Officer

Dr. Zhengzhao "Johnny" Luo (City College)

Dr. William B. Rossow (City College)

Dr. Allan Frei (Hunter College)

Supervisory Committee

THE CITY UNIVERSITY OF NEW YORK

Abstract

STUDY OF TROPICAL DEEP CONVECTIVE PROCESSES AND WATER VAPOR VARIATIONS USING NASA A-TRAIN DATA AND GEOSTATIONARY SATELLITE OBSERVATIONS

by

Hanii Takahashi

Adviser: Professor Zhengzhao "Johnny" Luo

The theme of this dissertation is to use various satellite observations to seek new insights into our understating of tropical deep convective processes and water vapor variations. Three subjects are investigated: 1) observational determination of level of neutral buoyancy (LNB) for deep convection, 2) characters and life stage view of tropical overshooting convection (OSC), and 3) variations of water vapor and clouds during East Pacific (EP)- and Central Pacific (CP)-El Niños.

The first study conducts a near-global survey of LNB for tropical deep convection using CloudSat (LNB_observation) and makes comparison with the corresponding LNB based on the parcel theory using ambient sounding (LNB_sounding). The principal findings are as follows: First, although LNB_sounding provides a reasonable upper bound for convective development, ambient sounding contains limited information for predicting the actual LNB. Second, LNB_sounding significantly overestimates the "destination" height level of the detrained mass. Third, LNB_observation is consistently higher over land than over ocean, although LNB_sounding is similar between land and ocean, suggesting some fundamental differences between land and ocean convection.

The second study uses CloudSat data together with ISCCP CT to study tropical OSC properties and the convective systems in which they are embedded. Our results find that, nearly 21 % of tropical deep convection is overshooting; the occurrence frequency is only slightly higher over land (~ 50.2 %) than over ocean (~ 49.8 %). Various proxies of convective strength are analyzed showing consistently that continental OSC is stronger than the oceanic counterpart. Moreover, majority (2/3) of the OSC occurs during the growing stage of the convective systems. About 1/3 occurs during the mature stage, which are more abundant over land during noontime.

The third study shows that EP- and CP-El Niño events produce different patterns of water vapor and cloud anomalies over the tropical ocean. Regression of water vapor anomalies onto the Niño-3.4 sea surface temperature shows a clear "upper tropospheric amplification" of the fractional water vapor change. Furthermore, water vapor and cloud anomalies in different circulation regimes are examined. Finally, Geophysical Fluid Dynamics Laboratory AM2.1 model simulations of water vapor and clouds are compared with the satellite observations.

Acknowledgments

I would like to express my sincere gratitude to **Dr. Zhengzhao "Johnny" Luo** for his professional guidance, continuous encouragement, and academically as well as mentally generous support throughout my graduate studies. I have always felt how lucky I am to be his graduate student. It was absolutely my pleasure to work with Dr. Zhengzhao "Johnny" Luo.

My gratitude and appreciation also go to my dissertation committee, **Dr. William B. Rossow and Dr. Allan Frei** for providing profitable discussion and careful revising.

I deeply appreciate **Dr. Hui Su** and **Dr. Jonathan Jiang**, whose mentoring skills and whole-heartedly support greatly helped me in time and in need.

Special thanks to **Jeyavinoth Jeyaratnam** for helpful support during my graduate studies. I appreciate not only for computational assistance but also for trustworthy friendship.

I also thank especially **Patrick Alexander** and **Juan Pinales**. They did not spare their time and efforts to give suggestion and correction to the manuscript.

Many thanks to my colleagues **Amelia Prasad**, **Erik Orantes**, **Nicholas Gao**, **Rajashree Datta**, **Ricardo Anderson**, and **Zena Marchant** for helping make my student life meaningful and enjoyable.

I want to thank my dear friends **Aya Yasuda**, **Dr. Bruce J. Shockey**, **Chizuko Midori**, **Dr. Eric J. Sargis**, **Katherine Yee**, **Kaori Tsukui-Shockey**, **Macarena Ortiz**, **Mari Ohara**, **Dr. Robert P. Thurstans**, and **Yoko Anderson**, who have always trusted, motivated, and supported me as if I were family.

Last but not least, I am grateful to my family; **Dr. Go Takahashi**, **Eba Takahashi**, **Prof. Stefan Wundt, Hitora Takahashi, and Dev Kumar Baniya**. They have supported me such a long time, even as I have been far from home. Without them, I would not have been able to build my academic career.

Table of Contents

List of Tables

List of Figures

Chapter 1

Introduction

1.1. Background and review

It has been half a century since the "hot tower" hypothesis, originally proposed by Riehl and Malkus (1958), stated that the "undiluted cloud towers" over the "equatorial trough zone" were capable of transporting heat from the planetary boundary layer (PBL) to the upper troposphere (UT). From a historic perspective, "hot tower" concept came about as a by-product of the study of heat balance in the equatorial trough zone, where excess latent heat is transported equatorward (in the opposite direction of general heat transport) by the lower-level trades, and then changes to sensible heat and potential energy during ascent. Riehl and Malkus (1958) found that the moist static energy ($MSE \equiv CpT + gz + L_v q$, where Cp, T, g, z, L_v, and q are specific heat of dry air, temperature, gravitational acceleration, height, latent heat of condensation, and specific humidity, respectively) decreases with height until 600–500 hPa and then increases above 400 hPa in the equatorial zone. Therefore, it is impossible to transport energy upward through mean vertical motion because air will travel counter-gradient to *MSE* from 400 hPa up and will become negatively buoyant. To solve this, Riehl and Malkus (1958) proposed the hot tower concept that convective "tubes" or "express elevators" (instead of large-scale air motion) pump energy upward. They further estimated that about 1500–2500 active cumulonimbus hot towers having undiluted updraft of 2–4 m/s and a diameter of 2–4 km are needed in the tropical trough region in order to meet energy balance requirements (Riehl and Malkus 1958; Fierro et al., 2009). Although the first weather satellites launched showed that mesoscale organization of convection is abundant in the equatorial trough zone, there was only one ideal model of a hot

tower, that of a "skinny undiluted tower," in the 1960s. The Global Atmospheric Research Program Atlantic Tropical Experiment (GATE) and the Monsoon Experiment (MONEX) were carried out in the 1970s to investigate hot towers using precipitation radar, instrumented aircraft, and radiosondes (Houze, 2003). Gradually, it has been established that hot towers can exist in many forms: some are isolated "skinny chimneys" but most others are embedded in larger-scale convective systems called mesoscale-convective systems or MCSs (Tao et al., 2003, Houze 2003).

The concept of "skinny undiluted towers" prevailed through the 1970s. Using new data, Riehl and Simpson (1979) reanalyzed the concept of vertical energy transported by undiluted hot towers and concluded that the results largely agreed with the Riehl and Malkus (1958) study. However, more recent results from aircraft and satellite observations and model simulations do not support the existence of such undiluted updraft cores; convection interacts with the environment in complicated ways in real world and thus dilution from the environment through entrainment seems to be ubiquitous (Zipser, 2003; Houze, 2003; Fierro et al., 2009). Therefore, recent studies suggest a slight modification of the original definition of hot tower by allowing some dilution from the environment as long as convection can reach near the UT outflow layer (~12km), fulfilling the purpose of transporting energy from the PBL to the UT (Fierro et al., 2009). Although this subject has been studied for more than 50 years, many of the details still remain elusive. The main purpose of this thesis is to elucidate some of the details pertaining to tropical deep convection using a host of satellite observations.

1.2. Motivation

Tropical overshooting convection (OSC) has received a great deal of attention, in part because of its potential to have a high occurrence of hot towers, which force clouds to continue to ascend, even after losing buoyancy (i.e., after passing the level of neutral buoyancy or LNB). Overshooting tops are able to penetrate into or even beyond the tropical tropopause layer (TTL ~ 14–18.5 [km]), where they act as a "gate to the stratosphere" for atmospheric tracers penetrative (Fueglistaler et al., 2009). A single occurrence of OSC has more influence on the water content, chemical composition, and thermodynamics of UT/LS (lower stratosphere) than frequently occurring non-convective slow ascents (Küpper et al., 2004; Kuang and Bretherton, 2004). It is known that moisture distributions within the tropical UT and LS are highly controlled by OSC (Danielsen, 1982; Sherwood and Dessler, 2000; Sherwood et al., 2003; Kuang and Bretherton, 2004). However, the location and rate of convective mass outflow in the TTL and LS are currently not well known (Fueglistaler et al., 2009), leading to difficulty in understanding the exact role OSC plays in controlling UT/LS moisture budgets. In fact, the question of whether OSC rehydrates (Corti et al., 2008; Khaykin et al., 2009) or dehydrates (Danielsen, 1993; Sherwood and Dessler, 2000; Holton and Gettelman, 2001) the TTL has been highly debated. A few studies have reported that both hydration and dehydration occur under different circumstances (Jensen et al., 2007; Hassim and Lane, 2010). Several adaptive scenarios have been proposed to explain the variation of UT/LS moisture budgets by OSC, but the definitive evidence needed to corroborate these two hypotheses has been lacking. Global surveys of cloud properties associated with OSC are also still rather incomplete.

Traditionally, satellite studies of convection have been conducted through birds-eye views of cloud tops based on passive sensors (e.g., infrared radiation (IR) satellite). Now, recent

launches of active sensors (such as TRMM precipitation radar in November 1997 and CloudSat in April 2006) provide us with new information, namely a detailed vertical cross-sectional view of convection. In this regard, we have an opportunity to study tropical deep convection from a new perspective. Moreover, water vapor is considered as an important component of the atmosphere, which interacts closely with convection. Combining data from another set of A-Train sensors, the Atmospheric Infrared Sounder (AIRS) and the Microwave Limb Sounder (MLS), we are able to examine the vertical profiles of atmospheric water vapor, temperature, and cloud ice content from surface to UT/LS. The study of water vapor distribution, especially for the UT/LS water vapor, will potentially help us better understand the mechanism of OSC. This thesis thus capitalized on these new space-borne capabilities to seek new insights into our understanding of tropical OSC and water vapor.

The research detailed in this dissertation has three major challenges. First, the temperature profiles inside of clouds are not available from current satellite observations, making it hard to directly estimate cloud buoyancy. The most common method of estimating LNB is to use parcel theory based on sounding data, which provides a theoretical rather than a directly measured value of LNB. We will address this issue in Chapter 2 (see also section 1.3.1). Second, information about convective dynamics is similarly not available from remote sensing data. In fact, even active sensors such as radar cannot measure vertical velocity, which makes it hard to estimate the intensity of tropical deep convection. Airborne measurements may be used to derive vertical velocity within OSC. However, such data are limited in space and time, making a global-scale study close to impossible. So, satellite-based proxies are needed to describe convection intensity. Third, most advanced sensors are onboard polar-orbiting satellites that picture OSC as static snapshots and do not provide the important information of convective life cycles (e.g., the

time dimension), so observations from a time-resolving platforms is needed to interpret the snapshots. Our research addresses these three challenges and develops new methods to further advance our understanding of tropical OSC through a multi-sensor and multi-platform approach.

1.3. Problems and objectives

Three research subjects are investigated in this dissertation: 1) observational determination of LNB for deep convection and comparison with the prediction based on the parcel theory, 2) characters and life stage view of tropical OSC, and 3) vertical distribution of water vapor and clouds during two different types of El Niños: East Pacific –and Central Pacific. Each of the following sections represents an objective that will be addressed in subsequent sections.

1.3.1. Objective 1: Observational determination of LNB from CloudSat

The LNB is the altitude where the temperature of the air parcel is equal to that of the environment. Above the LNB, the temperature of an air parcel becomes colder than its ambient air, which causes negative buoyancy and impedes the ascension of the convection to a greater altitude. Hence, the LNB is an essential variable needed to study convection since it controls convective buoyancy and determines the final fate of convection (e.g., cloud height or the level where convection starts to detrain). The most common method of estimating LNB is to use parcel theory (Bjerknes, 1938) based on sounding data (LNB_sounding hereafter) since temperature profiles inside clouds are not available. Parcel theory describes the simple path of a rising air parcel (e.g., an air parcel rises along the dry adiabatic path until it becomes saturated, and then follows moist adiabatic path) assuming that there is no air mass interaction between the

air parcel and its surrounding environment, and that the pressure of an air parcel is equal to that of its surrounding environment at the same altitude (Manzato and Morgan, 2003). However, the parcel method is idealized in that it only accounts for the original condition of surface soundings, while neglecting the interaction between convection and its surrounding environment (e.g., convective entrainment). In reality, convective entrainment affects buoyancy in complicated ways and eventually convection finds its own effective LNB, where it emerges as detraining masses and developing anvils (LNB_observation hereafter). Therefore, it is remains to be determined whether the LNB can be realistically estimated from the parcel theory alone. In fact, a case study of the "level of maximum detrainment" (LMD) conducted by Mullendore et al. (2009) indicates that there is a gap between the actual detrainment profile in deep convection and the LNB from parcel theory.

LNB is one of several critical parameters needed to select overshooting features since OSC is defined as deep convection whose cloud top exceeds the corresponding LNB. Verification of the accuracy of LNB_sounding is thus the first important task we have to address. The original concept of LNB is therefore reconsidered here by introducing a new method for retrieval of LNB_observation directly from satellite remote sensing, namely, CloudSat observations.

In the first half of the analysis in Chapter 2, we make a comparison between LNB_observation and the corresponding LNB_sounding to evaluate the efficacy of the LNB_sounding for allocating the upper, lower, and maximum mass detrainment levels. Additional variables such as the height of deep convective cores, the highest point of the cores, convective system size, as well as convective core size are also analyzed and compared over land and ocean. In the second half of the analysis, we focus on understanding the difference between

the LNB_sounding and the LNB_observation with respect to entrainment rate (the rate of change of the mass flux into the plume with height) using an entraining plume model. The mean bulk entrainment rates predict the amount of dilution by the surroundings, which adds additional information necessary for understanding LNB_observation and land-ocean contrasts.

1.3.2. Objective 2: Tropical overshooting convection from a satellite perspective

OSC is usually composed of strong convective updrafts (whose vertical velocity is greater than, for example, ~1 m/s), which are organized in a convective region. The stratiform region, on the other hand, consists of dissipated older convective cells (whose vertical velocity is less than, for example, ~0.5 m/s). From a satellite perspective, it is not a trivial task to separate convective updrafts from stratiform regions because satellite measurements of vertical velocity are currently not available. IR imagery is the mostly readily available information on cold convective clouds. As a result, many previous studies have applied a threshold to IR brightness temperature (Tb) measurements to identify OSC (Gettelman et al., 2002; Rossow and Pearl, 2007; Bedka et al., 2010; Bedka et al., 2012). However, it is sometimes challenging to use IR imagery to find convective updrafts because they often appear as cold as stratiform precipitation or cirrus anvils that are attached to the core (Houze, 1997). Tropical Rainfall Measuring Mission (TRMM) Precipitation Radar (PR) data also has been used to analyze tropical OSC (Alcala and Dessler, 2002; Zipser, 2003; Liu and Zipser, 2005; Liu et al., 2007). Although TRMM provides a vertical profile of convective clouds, its transmission wavelength of 21.7 mm is only limited to measure large particles (e.g., precipitation-size particles) and thus fails to provide information at the top of deep convection where small particles exist. Here, we use CloudSat to study OSC. CloudSat CPR provides valuable new insight because, operating at 3.19 mm and having

sensitivity as high as about –30 dBZ, it is capable of capturing cloud-size particles smaller than those measured by the TRMM CloudSat CPR is also sensitive to precipitation-size particles, although attenuation becomes a serious problem in presence of heavy rain.

The definition of OSC has been discussed in many different ways in previous studies. Recently, Iwasaki et al. (2012) summarized several thresholds that determine the overshooting features, which is naturally connected to our first question: What is an effective way to select overshooting features from CloudSat? Furthermore, to enrich our knowledge of OSC, the study of convective dynamics (e.g., convective intensity) is critical. In this regard, we have to consider an alternative to the vertical velocity, in order to estimate convective intensity. This leads to the second question to be addressed: What could be a proper proxy to estimate convective strength from CloudSat?

Onboard a polar-orbiting satellite, CloudSat cloud profiling radar captures convection through a static image captured only twice a day (~1:30 a.m./p.m. equatorial crossing time). As a result, life cycle information is missed. The ISCCP CT database, on the other hand, is derived from 3-hourly geostationary satellite data that track every convective system from "birth" to "death" (except for smaller systems with radius < 90 km due to ISCCP spatial resolution) (Machado et al., 1998). The ISCCP CT database gives CloudSat snapshot view the missing time dimension so that we are able to identify the life stage of deep convection in which overshooting tops are embedded. Herein lies the third question to be explored: In which life stages (growing, mature or dissipating) of deep convection does OSC tend to be observed? To address the three above-mentioned questions, CloudSat together with ISCCP-CT data are analyzed to explore the mechanisms of tropical OSC, with convective evolution and dynamics in mind.

In the first part of Chapter 3, we analyze the climatology of OSC. Here, the occurrence frequencies of deep convection and OSC based on CloudSat are discussed and compared to previous studies. Relationships between cloud properties and proxies of convective intensity are examined and their land-ocean contrasts are explored. Further, we identify five regions where OSC are most frequently observed: central Africa, Amazon, tropical warm pool (TWP), eastern Pacific (E.P.) Intertropical Convergence Zone (ITCZ), and Atlantic ITCZ. Cloud properties are analyzed separately and their differences are discussed.

The second part of this Chapter focuses on convective evolution. Following Futyan and Del Genio (2007), we use two independent variables, minimum brightness temperature (min Tb) and maximum radius size (max R) from the ISCCP-CT data, as proxies to determine the life stages of convection. The distribution of min Tb, max R, and the system lifetime are discussed and the comparison of these variables over land and ocean are examined. Eventually, occurrence frequencies of OSC embedded in three stages are calculated and further comparison over land versus ocean and during local noon (13:30) versus local midnight (1:30) are made to determine what kind of environment OSC is likely to occur in. The proxies for convective strength at different life stages are examined in parallel.

1.3.3. Objective 3: Vertical distribution of water vapor during EP- and CP-El Niños

Building upon previous analyses to understand the processes involved in convection, here we look into the reasons for variations in water vapor, one of the most important variables driving convection. Of particular interest are spatial and temporal variabilities of water vapor in the atmosphere. The vertical distribution and interannual variability of UT/LS water vapor are especially important variables needed for studying the impact of deep convection.

A recent study by Su and Jiang (2013) (hereinafter referred to as SJ13) showed that the variations of tropical cloud vertical structure, cloud radiative forcing (CRF), and circulation during the 2006-07 El Niño (moderate East Pacific (EP) El Niño) are very different from those of the 2009-10 El Niño (strong Central Pacific (CP) El Niño or El Niño *Modoki*). Moreover, SJ13 found that the variations of clouds and circulation during the two El Niños are more dominated by the magnitude than the pattern of anomalous SST. To further identify the different characteristics of the two types of El Niños, it is of interest to investigate variations in water vapor associated with the two ENSO events. Hence, we use the Aura Microwave Limb Sounder (MLS, above 300 hPa) and Aqua Atmospheric Infrared Sounder (AIRS, below 300 hPa) to examine the variation of vertical distribution of water vapor during the 2006–07 and 2009–10 El Niños. It is known that clouds, water vapor, and SST are closely coupled (e.g., Su et al., 2006). In this regard, water vapor anomalies during two different types of El Niños and their relation to clouds are analyzed.

In the first part of Chapter 4, we try to answer the question of how the two different types of El Niño events produce different patterns of water vapor anomalies over the tropical ocean. First, water vapor anomalies during the 2006–07 and 2009–10 El Niños are analyzed and comparisons are made in terms of tropical mean, zonal mean, and meridional mean. Subsequently, tropical water vapor anomalies in different circulation regimes are examined. Following Bony et al. (2004), we use mid-tropospheric vertical pressure velocity at 500 hPa or ω_{500} as a proxy of local dynamic conditions to seek the relationship between the variations of water vapor and large-scale circulation. We use ω_{500} from the European Centre for Medium-Range Weather Forecasts (ECMWF) ERA-interim reanalysis dataset. How sensitive water vapor

anomalies during the 2006–07 and 2009–10 El Niños are to the dynamic and thermodynamic structure of the atmosphere is the main question with which we concerned ourselves.

Regressions of water vapor mixing ratio anomalies and relative humidity (RH) anomalies onto the Niño-3.4. SST (5°S–5°N and 190–240°E) are conducted in the second part of this study. The vertical profiles of regression coefficients for the fractional change of water vapor (the ratio of the variation in specific humidity to the layer-averaged specific humidity) and RH are further examined separately over the western Pacific (10°S–10°N and 100–150°E) and the central Pacific (10°S–10°N and 160–200°E), together with those for the whole tropics (30°S–30°N). The western Pacific and the central Pacific are the regions where distinct negative and positive cloud anomalies are observed, respectively, during the two ENSO events. Finally, Geophysical Fluid Dynamics Laboratory (GFDL) AM2.1 model simulations of water vapor and clouds are examined and compared with the satellite observations. Our chief question here was how well the model reproduces the pattern and magnitude of water vapor and cloud anomalies in response to the two El Niño events.

1.4. Arrangement of the thesis

In Chapter 2, we introduce the methodology to estimate LNB_observation directly from CloudSat data. The importance of this analysis is to reconsider the validity and applicability of LNB_sounding. We select deep convection cases whose convective cores are attached to well-developed anvil clouds. LNB_observation is estimated based on the height of the selected anvils and LNB_sounding is calculated from ECMWF-AUX product from ECMWF operational analysis interpolated in space and time to the CloudSat track. To cover the whole range of the convective detrainment level, we define three LNB_observations: the highest detrainment level

(LNB_CTH), the lowest detrainment level (LNB_CBH), and the maximum mass detrainment level (LNB_maxMass). Our analysis is focused on the whole tropics region (30°S–30°N), but the methodology and analysis could also be applied to mid-latitudes.

In Chapter 3, we analyze CloudSat together with ISCCP-CT data to explore the mechanisms of tropical OSC, taking convective evolution and dynamics into account. There are two key points of this study. First, we take advantage of two different types of satellites, a polar-orbiting satellite and a geostationary satellite, to add the missing time dimension to an analysis of convective properties. Second, we use convective properties from CloudSat as proxies for convective strength to better understand the dynamics of OSC.

In Chapter 4, AIRS and MLS are used to study the entire vertical profile of water vapor from the surface to the UT/LS. We examine the variation of the vertical distribution of water vapor during the 2006–07 and 2009–10 El Niños together with GFDL AM2.1 model simulations. Here, we aime to explore the different atmospheric responses to 2006–07 and 2009–10 El Niños with respect to water vapor and clouds. To achieve this purpose, we discuss two questions: 1) How do the distributions of water vapor and clouds during 2006–07 (moderate EP El Niño) differ from those during 2009–10 (strong EP El Niño)? and 2) How well do the results between the model and satellite observations agree with each other?

A summary, and discussions of limitations and future work are presented in Chapter 5.

Chapter 2

Observational Determination of LNB form CloudSat

The content of this chapter also appeared in *Geophys. Res. Lett*., 39, L15809, doi:10.1029/2012GL052638

2.1. Introduction

Level of neutral buoyancy (LNB) is a critical parameter for understanding convection because it sets the potential vertical extent for convective development. Occasionally, strong convective turrets overshoot the LNB and may even penetrate into the stratosphere. In this case, knowledge of LNB provides important information for defining the overshooting features.

The classic definition of LNB is derived from the parcel theory by lifting a near-surface air parcel adiabatically to the upper troposphere where the air parcel starts to lose buoyancy. It can be estimated from the ambient sounding without having to observe any actual convective cloud development. In reality, however, convection interacts with the environment in complicated ways and will eventually manage to find its own effective LNB where it ceases to ascend and starts to detrain masses. The parcel theory may not be able to accurately predict *a priori* the effective LNB for each individual convective cloud; only the convective cloud itself knows this level and will manifest it through the development of cirrus anvils.

Mullendore et al. (2009) used a case study from the Tropical Rainfall Measuring Mission (TRMM) Large-scale Biosphere-Atmosphere (LBA) field campaign to show that the level of maximum detrainment of an observed squall line (which can be interpreted as the cloud's manifestation of the effective LNB) is significantly lower than the LNB derived from the

sounding data. However, no global analysis has been done to generalize the conclusion. This present study corrects the situation by conducting a near-global survey of the effective LNB using satellite observations (LNB_observation hereafter) and comparing it to the LNB based on the ambient sounding (LNB_sounding hereafter). The difference between the two is indicative of the underlying convective processes (e.g., dilution from entrainment of environmental air). A near-global survey is an important first step to generalize our understanding of these processes and their regional variations.

Previous studies used infrared brightness temperatures of the anvil clouds to estimate LNB (e.g., Bedka et al. 2010). This gives the uppermost level of the LNB. Analysis of CloudSat radar data, however, shows that anvil clouds develop over a thick layer of 4-5 km (e.g. Cetrone and Houze, 2009; Yuan and Houze 2010); within this thick layer, detrained masses are not uniformly distributed (Yuan et al. 2011). Further, Mullendore et al. (2009) found that radar reflectivity is well correlated with the convective mass detrainment. Therefore, radar observations contain rich information concerning where convective updrafts lose buoyancy and transition to detrainment and can thus be utilized to define LNB_observation in a more detailed manner than infrared brightness temperatures.

A number of previous studies have used space-borne radars to characterize anvil cloud climatology and structures and relate them to the convective systems that produce them (Cetrone and Houze 2009, Yuan and Houze 2010, Li and Schumacher 2010, Yuan et al. 2011). However, no attempt has been made to extract information on LNB and connect it to that based on sounding. The promising result from the case study by Mullendore et al. (2009) justifies a follow-up investigation of the problem using space-borne radar data. Here, we build upon these previous investigations and use CloudSat data to estimate LNB_observation and make

comparison with LNB_sounding derived from collocated operational analysis. Compared to TRMM precipitation radar (PR), CloudSat cloud profiling radar (CPR) has higher sensitivity to non-precipitating particles and allows for a more complete depiction of the anvil structures (Yuan and Houze 2010). We focus on the tropics (30S-30N) in the present study but the analysis method could be expanded to mid-latitudes. The rest of the paper is organized as follows. Section 2.2 describes the analysis methods and data used. Results and interpretations are presented in Section 2.3. Section 2.4 summarizes the study.

2.2. Data and analysis methods

CloudSat carries a 94-GHz, nadir-pointing, cloud profiling radar (CPR) sensitive to both cloud-size and precipitation-size particles. Its footprint is approximately 1.7 km along track and 1.3 km across track. The vertical resolution is 480 m, oversampled to 240 m. Stephens et al. (2008) provides an overview of the CloudSat data. Further details can be found from CloudSat Data Processing Center at http://cloudsat.cira.colostate.edu. In this study, we use 2B-GEOPROF data to estimate LNB_observation for deep convection. 2B-GEOPROF includes both radar reflectivity and cloud mask (cloud mask value $\geq$ 20 is used to identify clouds, which corresponds to reflectivity $\sim$ -30 dBZ). Ambient soundings are taken from ECMWF-AUX product containing temperature and moisture profiles from the European Centre for Medium-Range Weather Forecast (ECMWF) operational analysis interpolated in space and time to the CloudSat track. Data from June 2006 through December 2008 are analyzed.

The premise of this analysis is that cirrus anvils developing out of deep convection is a natural manifestation of where convection loses buoyancy and can thus be used as a proxy for LNB_observation. This gives us a clear feature of interest to search among cloud objects

observed by CloudSat. Figure 2.1 shows an example with a number of typical features readily identifiable: convective core is located near the center and overshoots above the rest of the cloud deck; cirrus anvils are well developed and expand horizontally.

Here we briefly describe our cloud selection method. Analysis starts from screening of each cloud object, defined as the area enclosed by cloud mask >20 in the CloudSat 2B-GEOPROF reflectivity data, similar to Riley and Mapes (2009) and Bacmeister and Stephens (2011). Given the CloudSat "curtain-like" sampling, one can think of a cloud object as the vertical cross section of a three-dimensional cloud. For each cloud object, we first look for the presence of deep convective core (DCC), which is defined as a CloudSat profile having 1) continuous radar echo from cloud top to within 2 km of the surface (i.e., the target cloud is rooted in the planetary boundary layer), and 2) echo top height (ETH) of the 10 dBZ greater than 10 km. These criteria are broadly in line with the characteristics of active convective cores as observed in Luo et al. (2008). Once the DCC is identified, we search horizontally on both sides of the cores for the attached anvils. Cloud base $\geq$ 5 km is required for anvils, following the statistics of the anvil base height in a previous study by Yuan and Houze (2010). We further impose the condition that the horizontal span of the cirrus anvil must be greater than 20 km to insure that the anvil is well developed and that enough information is available for estimating LNB_observation. Requiring the existence of the DCC makes it more likely that the detrainment is still fresh, minimizing the effect of ice particle sedimentation which may introduce a lower bias to the estimated LNB_observation. A total of 4,008 suitable cloud objects are selected from 2.5 years of CloudSat data.

For each selected convective objects, we define three forms of LNB_observation to capture the full range over which convective detrainment develops: 1) LNB is first estimated from the

cloud-top height (CTH) of the anvils, which we call LNB_CTH. This is the highest detrainment level and represents the destiny of the "lucky" parcels that are relatively less diluted during ascent or the ones that have the larger originating moist static energy in the planetary boundary layer. LNB_CTH can be readily compared to the infrared measurements, given the anvil is thick enough so that the infrared brightness temperature is representative of the cloud-top temperature. 2) Similarly, cloud base height (CBH) of the anvils is also estimated, referred to as the LNB_CBH. This is the lowest detrainment level and may come from the more diluted convective air parcels, or alternatively, the air parcels with lower originating moist static energy. LNB_CTH and LNB_CBH bracket the range of the effective LNB that can be determined observationally. 3) In between these two, we also estimate LNB using the height of the maximum radar reflectivity within the anvil column, which we call LNB_maxMass because Mullendore et al. (2009)'s case study shows that this level is well correlated with the maximum mass detrainment. LNB_maxMass is thus most relevant to convective mass transport.

Fig. 2.1 used an example to illustrate how various forms of LNB_observations are estimated. Multiple ways of defining the LNB_observation help capture the complex nature of convective detrainment. Together, they provide a more complete depiction of where convection loses buoyancy than IR data can do. For all the three forms of LNB_observation, calculation is done profile by profile first and then averaged over the first 20 km of the anvils. Choice of the first 20 km of the anvil is a compromise between the need to minimize random noises (longer samples preferred) and the concern of the bias due to ice sedimentation (shorter distance from the DCC preferred). According to Mullendore et al. (2009)'s case study, ice particle sedimentation would introduce a vertical displacement of ~ 1.2 km when ice particles travel 20 km from the initial detraining point, assuming mean outflow speed of 5 m/s.

LNB_sounding is calculated from the collocated ECMWF analysis profiles assuming pseudoadiabatic ascent from the planetary boundary layer. Given that the analysis tends to smooth out meteorological fields, we may expect some underestimation of LNB_sounding. However, the exact impact is difficult to quantity because of lack of collocated radiosonde data. We neglect the effect of hydrometeor loading and freezing. They tend to cancel each other: hydrometeor loading lowers LNB while latent heat of fusion increases LNB. Emanuel (1994) found a nearly exact cancellation using soundings over Florida in summer (their Fig. 14.4). To account for the uncertainty associated with the originating level, we launch the air parcel from both the surface and the level having the maximum moist static energy (MSE) between the surface and 925 hPa, following Liu and Zipser (2005). They are referred to as LNB_sounding1 and LNB_sounding2, respectively. LNB_souding2 is by definition higher than LNB_sounding1, but our results show that the difference between them is usually small (average < 30 m) so in discussions we only use LNB_sounding2. Finally, since this study focuses on tropical deep convection, we exclude in our analysis cases that are occasionally found to have LNB_sounding < 10 km.

2.3. Results and interpretations

Figure 2.2 shows the statistics of LNB_sounding and various forms of LNB_observation based on analysis of one year of CloudSat data. Also included are the statistics for the DCC heights and the highest point of the cores. Several findings deserve discussion. 1) LNB_CTH Vs LNB_sounding: LNB_CTH is slightly lower than LNB_sounding: the median values for LNB_CTH and LNB_sounding are, respectively, 13.41 km and 14.25 km. This suggests that LNB determined by the ambient sounding provides an overall reasonable upper bound for the

convective development. However, there is little one-to-one correspondence between LNB_sounding and LNB_CTH (both LNB_sounding and LNB_CTH span a large range from 10 to 16 km) as the linear correlation between them is only 0.29 (0.30 over ocean and 0.28 over land). So, although setting a reasonable upper limit, ambient sounding contains limited information content to accurately predict the height where actual convective clouds lose buoyancy and detrain mass. 2) LNB_maxMass Vs LNB_sounding: The median value of LNB_maxMass (10.68 km) is more than 3 km lower than that of LNB_sounding (14.25 km). Recall that LNB_maxMass measures the level where maximum mass detrainment occurs. This means that the majority of the convective air parcels lose their buoyancy at a level that is considerably lower than that set by the ambient sounding. From convective transport perspective, LNB_sounding is a significant overestimate of the "destination" height level of the detrained mass. The correlation between LNB_sounding and LNB_maxMass is 0.28 (0.30 over ocean and 0.25 over land), which again points to the limited value of using LNB_sounding to predict LNB_maxMass on a case-by-case basis. 3) LNB_CBH Vs LNB_sounding: LNB_CBH is further lower; the median value is only 8.41 km. Correlation between LNB_sounding and LNB_CBH is only 0.20 (0.21 over ocean and 0.16 over land). LNB_CTH (13.41 km) and LNB_CBH (8.41 km) bracket the height range over which tropical deep convection develops outflow and detrains mass.

Figure 2.2 also shows that convective cores with the median height of 14.24 km generally overshoot the level set by LNB_CTH (13.41 km). The median value of the highest point of the DCCs reaches 14.95 km. These height levels associated with the cores are higher than the base of the tropical tropopause layer (TTL), which is generally considered as located at ~ 14 km (Fueglistaler et al. 2009). Hence, our results suggest that the DCCs have the potential to directly

participate in the stratosphere-troposphere exchange, while the anvils with the median top height at 13.41 km are mainly confined within the troposphere.

Some land-ocean differences are observed (Table 2.1). We first note that LNB_sounding is very similar between land (median: 14.27 km) and ocean (median: 14.23 km). However, all three forms of LNB_observations are higher over land than over ocean: the median values for land (ocean) LNB_CTH, LNB_maxMass, and LNB_CBH are, respectively, 13.76 km (13.29 km), 11.14 km (10.55 km), and 8.78 km (8.27 km). Student's t-test confirms that all the differences are statistically significant at 0.95 confidence level. So, outflow from land deep convection pushes closer to the height level set by the ambient sounding than the oceanic counterpart. This may be related to the land-ocean difference in convective intensity (e.g., Zipser et al. 2006): stronger updrafts in land convection may bring the ascending air parcels to greater altitude and detrain mass at a higher level.

In addition to the vertical dimension, land and ocean deep convection also exhibits some difference in horizontal size. From CloudSat radar data, we define the size of a cloud object as the horizontal span of the CloudSat profiles, following that by Luo et al. (2011). The median size of the land convective systems (including both anvils and cores) is 140 km and that of the ocean counterpart is 167 km. On the contrary, median size of the DCCs shows the opposite trend: 14 km for land convection and 10 km for ocean convection. Both differences are statistically significant at 0.95 confidence level. Although our definition of cloud size is somewhat different from previous studies using passive sensors (e.g., IR images), a qualitative comparison can still be made. A number of publications have shown that convective system over ocean is larger than over land. For example, Machado and Rossow (1993) arrived at this conclusion by conducting a global analysis of tropical cold cloud cluster (spatially-adjacent pixels in IR images with cloud-

top temperature colder than 245 K). On the other hand, larger cores for land convection than ocean convection have been documented in studies using precipitation radar (e.g., Liu et al. 2007) and *in situ* aircraft measurements (e.g., Lucas et al. 1994). Analysis of CloudSat data corroborate these previous work and further establish the fact that oceanic convective systems are bigger but the embedded convective cores are narrower.

The final "fate" of the updraft air parcels is closely related to their interaction with the environment. For example, entrainment of ambient air with lower moist static energy can significantly lower the effective LNB of these ascending air parcels. The difference between LNB_observation and LNB_sounding may thus be interpreted as a measure of the magnitude of the entrainment effect: the greater the entrainment rate, the larger the height difference. Here, we use a simple model (entraining plume model) to understand the differences between LNB_sounding and LNB_observation. Despite the simplified form, the entraining plume model is commonly used in GCM cumulus parameterization schemes in which cumulus convection is modeled as an ensemble of plumes with characteristic LNB and entrainment rates, each sharing a fraction of the total convective mass fluxes as determined by the parameterization's closure scheme (e.g., Arakawa and Schubert 1974). As observational equivalents, we may regard LNB_CTH, LNB_maxMass and LNB_CBH as representing the final outflow destination of three general types of "plumes": LNB_CTH (LNB_CBH) corresponds to the highest (lowest) reaching plume with the smallest (largest) entrainment rate and LNB_maxMass to the plume that has the largest share of the deep convective mass flux.

Following Luo et al. (2010), the entraining plume model is formulated as: $\frac{\partial MSE_p}{\partial z} = \lambda(MSE_e - MSE_p)$, where λ is the bulk entrainment rate (unit: %/km), and moist static energy (MSE) $\equiv C_pT + gz + L_vq$ (T, z and q are temperature, height and specific humidity,

respectively; C_p is the specific heat of dry air, g gravitational acceleration, and L_v the latent heat of condensation); subscripts p and e refer to properties of the in-cloud air parcel and of the environment, respectively. MSE_e can be estimated from the sounding data. We calculate λ iteratively by integrating the equation from the surface to the corresponding LNB_observation. The calculated mean bulk entrainment rates for LNB_CTH, LNB_maxMass, and LNB_CBH are, respectively, 3%/km, 6%/km and 10%/km. These numbers are in the similar range of the estimates given by Luo et al. (2010) for tropical deep convection. They may serve as an observational constraint for adjusting GCM cumulus parameterizations. For example, a recent study by Kim et al. (2011) showed that an improved simulation of ENSO variability can be achieved by setting a minimum allowable entrainment rate. Our results give some observational guidance concerning what minimum thresholds to choose.

There are also some land-ocean differences. The mean entrainment rates are slightly smaller over land than over ocean. For example, the corresponding entrainment rates for land (ocean) LNB_maxMass and LNB_CBH are, respectively, 6%/km (7%/km), and 9%/km (10%/km). This difference may be attributable to the size difference of convective cores: land convection tends to have larger convective cores, which provide better protection from entrainment dilution (Lucas et al. 1994). Our analysis of the DCC width supports this explanation (Table 2.1).

2.4. Summaries and discussion

This study revisits an old concept in meteorology – level of neutral buoyancy (LNB). The classic definition of LNB follows the parcel theory assuming no dilution by the surroundings; it can be simply derived from the ambient sounding (LNB_sounding). In reality, however, convection interacts with the environment in complicated ways. It will eventually find its own

effective LNB and manifests it through detraining masses and developing anvils (LNB_observation). In this study, we conduct a near-global survey of LNB_observation for tropical deep convection using CloudSat data and make comparison with the corresponding LNB_sounding. Three forms of LNB_observation are defined to reflect the fact that convective detrainment occurs over a broad range of heights: LNB_CTH refers to the highest detrainment level, LNB_CBH the lowest detrainment level, and LNB_maxMass corresponds to the level of maximum mass detrainment. The principal findings are as follows:

1. LNB_sounding provides an overall reasonable upper bound for convective development. However, linear correlation between LNB_sounding and LNB_CTH is only 0.29, suggesting that ambient sounding alone contains limited information content to accurately predict the actual LNB where convective clouds lose buoyancy and detrain mass.
2. LNB_maxMass, which measures the level of maximum mass detrainment, is more than 3 km lower than LNB_sounding. So, LNB_sounding is a significant overestimate of the "destination" of convective mass transport. Correlation between LNB_maxMass and LNB_sounding is only 0.28.
3. All three forms of LNB_observation are higher over land than over ocean, while LNB_sounding is very similar between land and ocean. So, deep convection over land tends to detrain mass at a higher level and the outflow from land convection pushes closer to the height level set by the ambient sounding. Moreover, it is noticed that oceanic deep convective systems are larger than their land counterparts, but the embedded convective cores in the oceanic systems are smaller.

4. The difference between LNB_sounding and LNB_observation is closely related to convective entrainment because entraining ambient air with lower moist static energy will lower the LNB_observation. Using an entraining plume model, we estimate the bulk entrainment rates (λ) associated with all three forms of LNB_observation: the mean λ values for LNB_CTH, LNB_maxMass and LNB_CBH are, respectively, 3%/km, 6%/km and 10%/km. The estimated entrainment rates can serve as observational constraints for adjusting GCM cumulus parameterization.

Table 2.1: Median value of LNB_sounding, LNB_CTH, LNB_maxMass, LNB_CBH, DCC height, and the highest point of DCC [Unit: m]. Also shown are the sizes of the DCC and of the whole system [unit: km], as well as the total number of selected convective cloud objects. Values in the parentheses are the corresponding standard deviations.

Median (STD)	LNB_sounding1	LNB_sounding2	LNB_CTH	LNB_maxMass	LNB_CBH
All	14,219 (1,203)	14,247 (1,163)	13,406 (1,365)	10,680 (1,342)	8,409 (1,495)
Ocean	14,229 (1,141)	14,234 (1,135)	13,293 (1,358)	10,548 (1,315)	8,272 (1,473)
Land	14,185 (1,388)	14,268 (1,254)	13,756 (1,327)	11,141 (1,337)	8,783 (1,527)
Median (STD)	DCC-height	Highest DCC	System Size	DCC Size	No. of cases
All	14,237 (1,194)	14,951 (1,204)	159.5 (159.7)	11 (25.7)	4008
Ocean	14,125 (1,168)	14,841 (1,186)	167.2 (165.1)	9.9 (25.1)	3087
Land	14,654 (1,198)	15,373 (1,176)	139.7 (136.5)	14.3 (27.5)	909

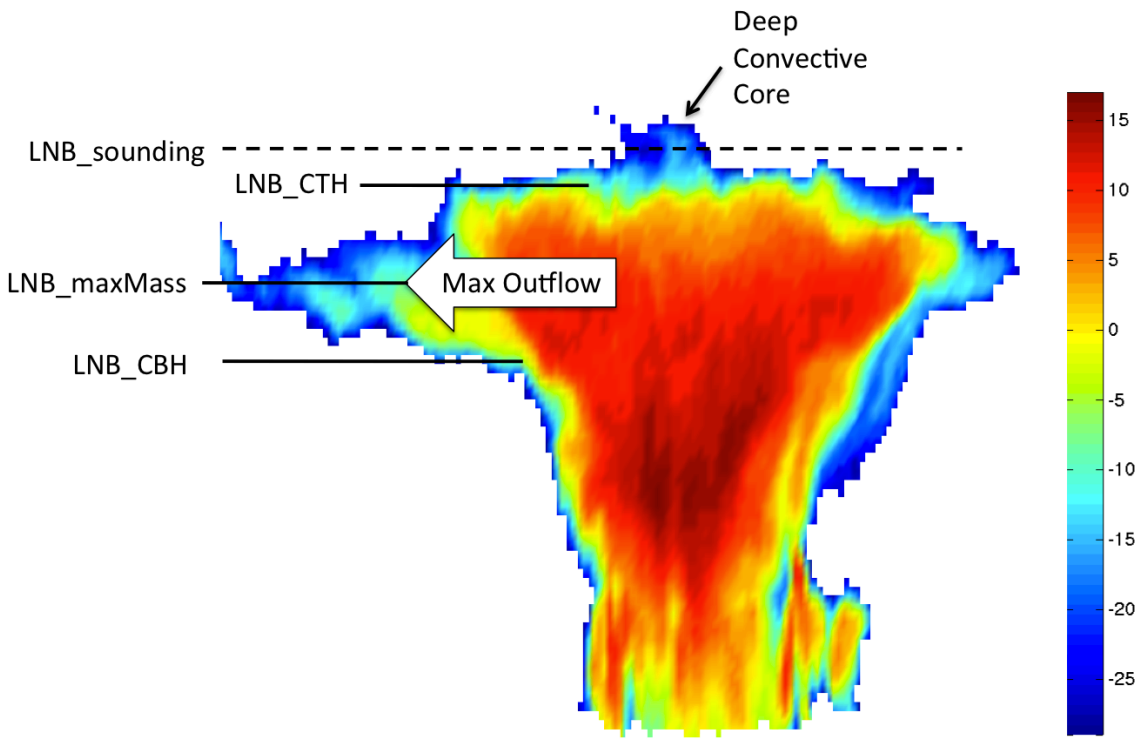

Figure 2.1. CloudSat radar reflectivity profile of a tropical deep convective cloud observed on February 24 2007 over Amazon (unit: dBZ). The size of the system is about 140 km and the highest point is about 17 km. Various forms of LNB_observation are marked up and illustrated using this example. LNB_CTH, LNB_maxMass and LNB_CBH refer to, respectively, LNB defined by anvil cloud top height (CTH), maximum mass outflow (determined by radar reflectivity) and anvil cloud base height (CBH). See text (the 4th paragraph of Section 2.2) for detailed explanation.

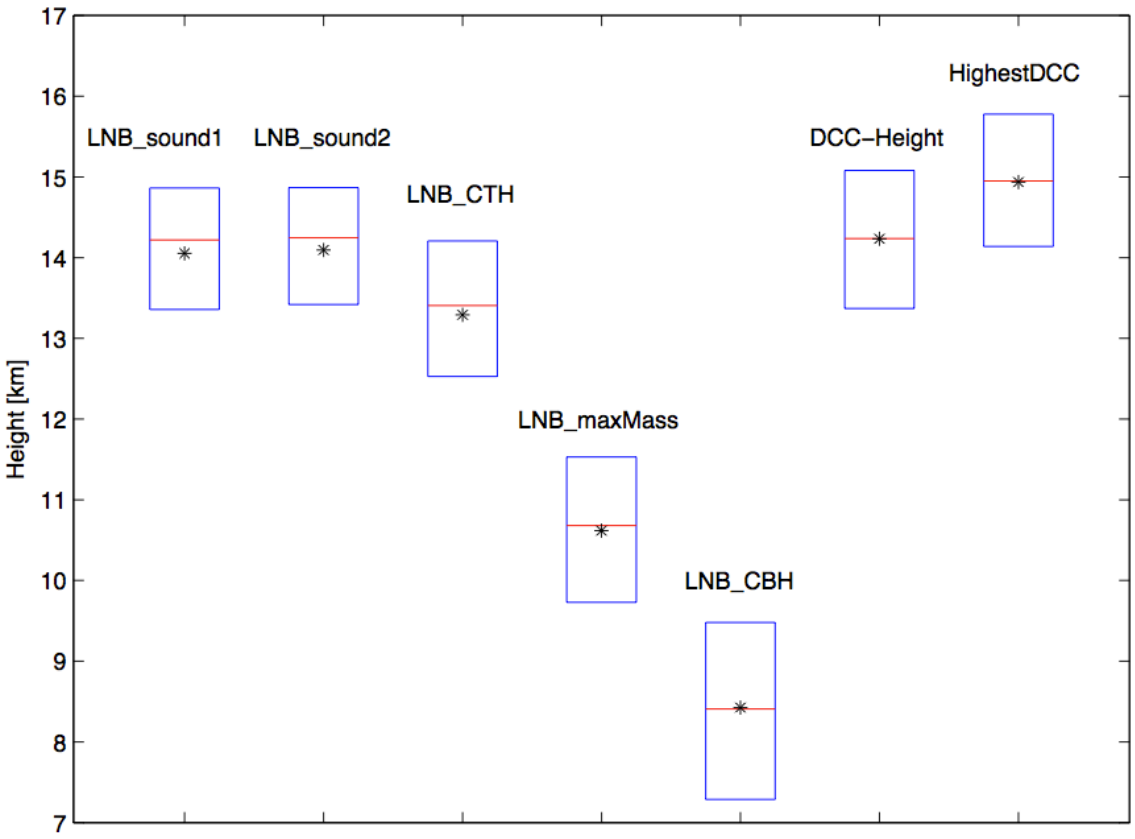

Figure 2.2. Box diagram for LNB_sounding, LNB_CTH, LNB_maxMass, LNB_CBH, height of DCC and of the highest point. The bottom and top of the boxes show, respectively, the 25% and 75% percentile. The central lines show the median and stars inside the box show the mean.

Chapter 3

Tropical Overshooting Convection from A Satellite Perspective

3.1. Introduction

It has been well established that tropical deep convective clouds are an important agent in transporting energy and moisture (and other trace gases) from the planetary boundary layer to the upper troposphere (e.g., Riehl and Malkus 1958; Riehl and Simpson 1979). Of special interest is a small subset of deep convection that overshoots. Overshooting convection (OSC) has the potential of penetrating into the tropical tropopause layer (TTL) or even directly into the lower stratosphere. Considerable debates have been seen in the literature concerning the exact role played by tropical OSC in affecting the lower stratospheric heat and moisture (e.g., Sherwood and Dessler 2000; Küpper et al. 2004; Kuang and Bretherton 2004). One particularly uncertain area concerns where and at what rate convective mass outflow occurs in the TTL and lower stratosphere (Fueglistaler et al. 2009). On the one hand, tropical OSC is a less-frequently occurring phenomenon (e.g., Luo et al. 2008) so its importance in transporting mass and constituents could be overshadowed by slow but ubiquitously occurring ascent in TTL, as shown in Küpper et al. (2004). But on the other hand when OSC occurs, it takes up a disproportionately intense form and profoundly affects the thermodynamics and chemical compositions of the TTL and lower stratosphere (Kuang and Bretherton 2004).

Understanding these important influences requires, in part, ways of observing the tropics-wide distribution of OSC as well as their properties and behaviors. A number of satellite-based studies have been conducted in the past. Using IR brightness temperature (TB) measurements, Gettelman et al. (2002) described the global distributions of tropical deep convection that

penetrates into the lower stratosphere. Bedka et al. (2010; 2012) specifically examined the overshooting tops with TB lower than the surrounding anvil clouds by some thresholds. Rossow and Pearl (2007) took a different approach by characterizing the nature of the convective systems that contain cold pixels representing overshoots into the stratosphere; it was found that most of them are larger, organized convective systems. Hong et al. (2005) utilized high-frequency passive microwave measurements (~183 GHz) to identify tropical OSC based on the scattering effect in the microwave due to large ice particles lofted by strong convective motion. Liu and Ziper (2005) and Liu et al. (2007) examined the vertical structure and intensity of penetrative deep convection using data from the Tropical Rain Measuring Mission (TRMM) Precipitation Radar (PR) operating at 13.8 GHz that is sensitive to moderate to heavy rains.

Recent launch of CloudSat, which carries with it a 94-GHz cloud-profiling radar sensitive to both cloud- and precipitation-size particles, provides another opportunity to study OSC. Luo et al. (2008) used a combination of CloudSat radar reflectivity profiles and MODIS (Moderate Resolution Imaging Spectrometer) IR brightness temperatures to infer life cycle of tropical penetrating deep convection. Iwasaki et al. (2010; 2012) analyzed CloudSat, CALIPSO (Cloud-Aerosol Lidar and Infrared Pathfinder Satellite Observations), and MODIS to study the mixing of overshoots with the stratospheric air. This paper builds upon these previous works and further studies tropical OSC using CloudSat data. An important aspect of this current study is the combination of CloudSat and geostationary satellite observations, the latter being obtained from the International Satellite Cloud Climatology Project **(**ISCCP) Convection Tracking (CT) database. Recent publications by Luo et al. (2009; 2010) have shown that to understand the snapshot views of convection as obtained from polar-orbiting satellites (CloudSat being just one example), it is important to place them in a proper dynamic context because different snapshots

capture convection at different life stages. Geostationary satellites provide the capability of observing the full lifecycle of the convective clouds, which CloudSat only sees with one passing glimpse at a certain life stage. Therefore, we analyze CloudSat depiction of tropical OSC properties and behaviors with convective evolution and dynamics in mind, adding the otherwise missing time dimension to the CloudSat observations from using ISCCP CT data.

After this introduction, we will describe data and methodology in Section 3.2. Analysis results and interpretations are presented in Section 3.3. Section 3.4 summarizes the study.

3.2. Data and methodology

A little more than two years (Sep 2006 – June 2008) of CloudSat data (2B-GEOPROF and ECMWF-AUX products), together with the International Satellite Cloud Climatology Project (ISCCP) Convection Tracking (CT) database, are used to characterize tropical overshooting convection and the cloud systems in which they are embedded. Although CloudSat data extend beyond June 2008, ISCCP CT data have not yet been updated. September 2006 – June 2008 is the overlapping period. Given the large number of cases observed (~680,000), results coming out of the 2.3 years of data should be statistically robust. When ISCCP CT is extended, we plan to update the analysis.

3.2.1. Satellite observations

CloudSat is a member of the A-Train constellation, which consists a suite of polar-orbiting satellites with an equator crossing time ~1:30 am/pm (Stephens et al., 2008). The CloudSat carries a 94-GHz cloud profiling radar (CPR), which is sensitive to both cloud-size and precipitation-size particles. The footprint of CloudSat is about 1.7 km along track and 1.3 km

across track, and the effective vertical resolution is 480 m with oversampling at 240 m resolution. Further details about the CloudSat mission can be found in Stephens et al. (2008) or the CloudSat Data Processing Center webpage at http://cloudsat.cira.colostate.edu. Here, we mainly use 2B-GEOPROF and ECMWF-AUX data products to characterize tropical OSC. The former product offers cloud mask and radar reflectivity and the latter provides temperature and moisture profiles from the European Centre for Medium-Range Weather Forecasts (ECMWF) operational analysis interpolated in time and space to the CloudSat track.

The ISCCP CT database is derived from geostationary satellite data. Based on the ISCCP pixel-level data (DX), spatially sampled at 30 km intervals, a convective system database has been constructed by clustering all adjacent cold IR pixels with brightness temperature (TB_{IR}) < 245 K (Machado and Rossow 1993). Such clusters are referred to as Convective Systems (CSs), whether or not they actually contain convective clouds. A further test identifies Convective Clusters (CCs) as adjacent cloud pixels with TB_{IR} < 220 K. CSs are usually irregular in shape, so to make the results tractable, Machado et al. (1998) modeled each CS as ellipse and recorded the structural and radiative properties. Once CSs are identified, Machado et al. (1998) developed a procedure to track the evolution each individual CS. This makes the Convective Tracking (CT) dataset that includes the whole CS family whose radiuses are at least 90 km (about 30 pixels in the ISCCP DX dataset). The ISCCP CT product currently covers the period from July 1983 through June 2008. Figure 3.1 shows the tracking of a tropical CS (represented by the green ellipse) over a period of 12 hours. One can clearly see the propagation of the CS to the west as well as the evolution of CS structure and properties (e.g., popping out of new convective cells). CloudSat happens to pass by this CS at around 12 Z, capturing the vertical structure of the system at this instant. The data and the document describing the dataset are available at

http://isccp.giss.nasa.gov/cgi-bin/CT.pl.

3.2.2. Selection of OSC

OSC can be identified from satellite observations using a number of methods. The most commonly used method draws upon IR measurements because overshoots appear as cold pixels in the IR imageries (e.g., Gettelman et al. 2002, Rossow and Pearl 2007, Bedka et al. 2010; 2012). Passive microwave measurements can also be used to identify overshooting deep convection (Hong et al. 2005). Active sensing systems provide the profiling capability, and in the past, TRMM PR observations have been utilized to study the penetrative deep convection (e.g., Alcala and Dessler 2002; Liu and Ziper 2005). But since TRMM PR is only sensitive to large precipitating particles (sensitivity at ~18 dBZ), it generally underestimates the heights of the overshoots. In this study, we use measurements from the CloudSat CPR.

By definition, OSC refers to convective plumes that overshoot the level of neutral buoyancy (LNB). So, the first step is to find a proper way to define the LNB. The classic definition of LNB is derived from the parcel theory by lifting a near-surface air parcel adiabatically to the upper troposphere where it starts to lose buoyancy (called LNB_sounding). LNB can also be determined observationally by observing the actual outflow of deep convection (called LNB_observation). Takahashi and Luo (2012) compared the two versions of LNB using both sounding (ECMWF analysis) and observations (CloudSat); it was found that LNB_sounding is a reasonable upper bound for LNB_observation, with the former being ~ 800 m higher than the later. Considering that using LNB_observation severely limits the sample size (only 4,800 cases are found for 2.5 years of CloudSat data, mainly from the west pacific) for global survey of OSC, in this study we calculate LNB from the ECMWF-AUX data (i.e., LNB_sounding) and use it as

the reference level for selecting OSC: any convective tower observed by CloudSat that extends above the corresponding LNB by some threshold is defined as OSC. For the tropics (30S-30N), LNB for the selected OSC ranges from 12.3 to 13.7 km depending on locations (Table 1).

The exact OSC selection procedure goes as follows: First, deep convection is identified from CloudSat 2B-GEOPROF data in a way similar to Takahashi and Luo (2012). The requirements are: 1) cloud-top height (CTH) $\geq$ 10000 m, 2) cloud-based height (CBH) $\leq$ 2000 m, 3) continuity in radar echo from CBH to CTH to exclude non-convective, layered clouds. CPR Cloud Mask $\geq$ 20 (20 or higher indicates high confidence in cloud detection; note cloud mask value is not to be confused with radar reflectivity) is required, as in Riley and Mapes (2009) and Bacmeister and Stephens (2011). Second, the corresponding LNB is calculated from collocated ECMWF-AUX data assuming pseudo-adiabatic ascent from the planetary boundary layer. Finally, OSC is defined as any convective profile from CloudSat CPR with CTH > LNB + δ, where δ = 500m. Choice of 500m for δ is meant to match previous studies such as Bedka et al. (2010). We have experimented δ from 0 to 1300m. The final choice of δ=500m provides OSC statistics that agree broadly with previous studies. Note that we do not use the tropical tropopause height as the reference level for selecting OSC. Thus, OSC as defined in this study (i.e., cloud tops higher than the corresponding LNB) may be different from penetrating deep convection (i.e., convection penetrating the TTL) as defined in other studies (e.g., Luo et al. 2008). Figure 3.2 gives an example how OSC is selected. The upper panel shows the IR brightness temperature (a proxy for cloud top temperature) from Moderate Resolution Imaging Spectroradiometer (MODIS). The dotted line indicates the CloudSat footprint. The lower panel shows the vertical distribution of radar reflectivity from CloudSat. The black line is the height of LNB, and the arrows point to the locations of the selected overshooting features.

3.2.3. Proxies of convective strength

CloudSat CPR offers some unique views of OSC. Its high sensitivity to both cloud and precipitating particles and profiling capability give a glimpse into the internal vertical structure of OSC and also allows for the identification of convective strength. Here, we define three proxies for convective strength. The first proxy is radar echo-top height (ETH) of large echoes. ETH of 0 dBZ (10 dBZ) is the highest altitude that 0 dBZ (10 dBZ) radar echo reaches. Strong updraft tends to produce a high ETH, i.e., large particles being lofted to greater altitude. The second proxy is called overshooting distance (OSD), defined as the difference between CTH (which roughly corresponds to the ETH of -30 dBZ) and LNB. OSD describes the extra distance by which a deep convective plume overshoots the corresponding LNB. Intuitively, it is indicative of the convective strength or intensity as stronger convective plumes overshoot higher. The extremely strong deep convection can penetrate directly into the stratosphere, much higher than the LNB (e.g., Luo et al. 2008). The third proxy is called cloud top-echo top distance (CTETD), which is defined as the distance between CTH and ETH of 0 dBZ and 10 dBZ. When convection is strong, both small and large particles are lofted to higher altitude, so CTH and ETH are similar (thus small CTETD). On the other hand, if convection is weak, large particles fall short of the cloud top resulting in large CTETD. Figure 3.3 uses schematics to illustrate these different proxies.

3.2.4. Definition of convective life stage

ISCCP-CT database gives CloudSat snapshot views the missing time dimension so that we are able to identify the life stage of CSs in which OSC is embedded, as illustrated in Figure 3.1. Following Futyan and Del Genio (2007), we use two independent variables, coldest IR

brightness temperature and size (radius) of the CS to determine the life stages of the convective system. We define it as the "developing stage" if the system has not reached the min TB_{IR} (i.e., highest CTH) of its lifetime, and the "dissipating stage" if the system has already passed its maximum size. The life stage between the "developing stage" and the "dissipating stage" is defined as the "mature stage". The rationale for the life stage classification is that CSs are expected to develop vertically first and then expands horizontally. To smooth out abrupt changes in minimum brightness temperature and radius, we apply a polynomial curve fitting and use F-test to determine the best order fit. Only CSs whose lifetimes are more than 6 hours (i.e., a minimum of 3 geostationary images) and radiuses are larger than 90 km have been used. Depending on the time at which CloudSat-observed OSC intercepts the ISCCP-CT data, it is assigned a given life stage – developing, mature, or dissipating. Figure 3.4 illustrates the overall methodology using an example of OSC embedded in the mature stage of the CS.

3.3. Results

3.3.1. Occurrence frequency of OSC and regional variations: CloudSat perspective

We first examine deep convection (DC) in general: the occurrence frequency of DC by CloudSat (see Section 3.2 for definition) is about 2.1 % over whole tropics (30°S to 30°N) (Figure 3.5, the 2nd panel). It is about 3.1 % if we only count 15°S to 15°N. This number is slightly lower than the statistics given by Luo et al. (2008), which is 3.9 % based on 2B-CLDCLASS data due to slightly different definition of DC. It should be noted that the CloudSat definition of DC, both ours in this paper and in 2B-CLDCLASS product, does not count the attached thick anvil because active sensors can effectively separate convective plumes from the anvils based on radar profiles. This is different from most IR-based definition where it is hard to

differentiate thick anvil from active convective plumes because they both show similar cold temperature.

OSC is a small subset of DC. Statistics of OSC depends on the choice of the reference level (i.e., LNB) and the overshooting distance (δ). Figure 3.5 (top panel) shows the climatology of LNB based on ECMWF analyses. Figure 3.5 also shows the occurrence frequency of OSC with different δ values: it varies from 0.24% to 0.65 % over 30°S-30°N and 0.36% to 0.97 % over 15°S -15°N when δ varies from 0 m to 1300 m (panels 3 – 6). Larger δ leads to fewer OSC. In this study, we use δ=500 m, following the reason described in the Section 2.2. Under this definition, the occurrence frequency of OSC is 0.46 % over 30°S -30°N (Figure 3.6, the 4th panel) and 0.69 % for 15°S and 15°N. So, considering that the DC occurrence frequency is 2.1% (30S-30N), our result shows that approximately 21 % of tropical DC has overshooting tops, which is comparable to the statistic given by Hong et al. (2005) who found that 26 % of tropical DC has overshooting tops.

Of particular interest are the OSC events that have potential to directly penetrate into the lower stratosphere. Luo et al. (2008) studied the convective life cycle and internal vertical structures of such penetrative deep convection. Here, our result shows that only ~1 % of tropical DC (i.e., ~0.0002 of the tropical region) has overshooting tops higher than 16.5 km, which is about the mean cold point tropopause defined by Gettelman and Forster (2002). This result is similar to the statistics as given by Luo et al (2008) and broadly agrees with Rossow and Pearl (2007), although the definition of OSC and DC differs among these authors. The exact role played by these penetrative deep convective events in terms of their impacts on the lower stratosphere energy and trace gases is not clearly understood (Fueglistaler et al. 2009).

Land-ocean contrasts are also investigated. For our definition of OSC, the occurrence

frequency is only slightly higher over land (~ 50.2 %) than over ocean (~ 49.8 %). At the face value, this seems to be somewhat at odd with previous work using TRMM PR, which found noticeably more OSC over land than over ocean (e.g. Liu and Ziper 2005). However, it should be emphasized that CloudSat PR with the sensitivity at ~ -30 dBZ sees small ice crystals at the top of OSC whereas TRMM PR with sensitivity at ~ 18 dBZ only detects precipitation-size particles. Liu et al. (2007) reconciled different views of OSC from TRMM PR and IR measurements. CloudSat-detected cloud tops are more similar to those by IR (i.e., small cloud particles), so its depiction of land-ocean contrast is comparable to that by Gettelmann et al. (2002) and Rossow and Pearl (2007). It is interesting to note that if we choose δ=900 m, that is, stricter criterion for selecting OSC, then land-ocean contrast starts to tilt more toward land (55.7 % for land and 44.4 % for ocean). This becomes more similar to the result from analysis of the TRMM PR data (Liu and Zipser, 2005; their Table 3 for the case using LNB_{sfc} as the reference height). Pushing δ to the extreme (1300 m), it becomes clear that OSC dominates over land (62.3 % for land and 37.7 % for ocean), suggesting that real intense OSC is more prevalent over land, consistent with results from TRMM (Liu and Zipser 2005) and passive microwave (Hong et al. 2005), which are more sensitive to large ice particles indicative of intense convective updrafts.

Another potentially important factor to consider when comparing our results to those by TRMM and IR is diurnal cycle. CloudSat makes measurements at around 1:30 am/pm local time. Tropical deep convection over land has strong diurnal cycle and the peak is usually in the late afternoon (Liu and Zipser 2008). Therefore, CloudSat probably underestimates the occurrence frequency of OSC over land. Deep convection over ocean, in contrast, has much smaller diurnal cycle (Liu and Zipser 2008) so less problem is expected over ocean. We will return to the issue concerning the diurnal cycle in Section 3.3 when ISCCP CT data are analyzed in conjunction

with CloudSat. ISCCP-CT data provide a full coverage of the diurnal cycle because they are based on geostationary satellite data.

Some regional differences in DC and OSC are worth discussing. Figure 3.5 shows that DC and OSC are most prevalent over the following fives regions: central Africa, Amazon, tropical warm pool (TWP), eastern Pacific (EP), Intertropical Convergence Zone (ITCZ), and Atlantic ITCZ (black boxes in Figure 3.5 define these regions). While the overall statistics shows little difference in OSC over land versus over ocean (50.2% versus 49.8%), the two land centers of action (tropical Africa and Amazon) have significantly more OSC than the three oceanic counterparts. The land-ocean difference in OSC can be examined in another way, that is, the percentage of DC that overshoots (or the ratio of OSC to DC). The percentages are, respectively, 34.5 %, 26.5 %, 15.6 %, 32.9 %, and 25.0 % over the five regions (tropical Africa, Amazon, TWP, E.P. ITCZ, and Atlantic ITCZ), showing that tropical Africa has the highest percentage and TWP has the lowest. Although DC in general is most abundant over Amazon and TWP, OSC is most frequently observed over Amazon and tropical Africa.

3.3.2. Convective properties associated with OSC

CloudSat CPR offers a unique view of OSC and their internal vertical structure, which have not been systematically documented before. Here, we analyze various parameters that are used to characterize cloud structure (e.g., CTH), convective intensity (the three proxies defined in Section 2.3: ETH, OSD, and CTETD) and convective environment (e.g., LNB), as well as the relationship among them.

Table 1 summarizes these parameters associated with OSC for the whole tropics, land and ocean, and the five regions as defined in Figure 3.5. In general, LNB is slightly higher over

ocean than land (13,085m versus 12,495m). CTHs for the OSC are similar over land and ocean (14,516m versus 14,591m). However, convective intensity is consistently stronger over land than over ocean as indicated by all three proxies: OSD, CTETD for 0 dBZ and CTETD for 10 dBZ. Among all five regions, tropical Africa shows the strongest convective intensity with the largest OSD and the smallest CTETD. OSC over the TWP has the weakest intensity based on these measures. The contrast in deep convection characteristics between tropical Africa and TWP has been studied by Liu and Zipser (2005) using TRMM PR; their results are qualitatively similar to our findings using CloudSat CPR, namely, stronger deep convection over tropical Africa and weaker convection in TWP. This suggests that CPR ETHs of 0dBZ and 10dBZ are indicative of convective strength, in a way similar to TRMM PR ETH. However, it should be pointed out that since CPR has the sensitivity down to -30 dBZ, it gives a more complete depiction of the whole envelope of the convective system than PR in the vertical dimension. For example, Table 1 shows that smaller cloud particles as represented by CPR CTH reach higher over TWP (15,169m) than tropical Africa (14,514m), although over tropical Africa, large rain-size particles as represented by ETHs of 10 dBZ (which are supported by strong updraft) ascend to higher altitude and closer to the cloud top compared to TWP.

Lucas et al. (1994) discussed possible reasons for stronger land convection: although the absolute values of CAPE do not differ too much between land and ocean convective environment, their shapes are different: oceanic convection has "skinny" CAPE (e.g., the associated positive area of CAPE is narrow), whereas continental convection tends to have "fat" CAPE (e.g., the associated positive area of CAPE is wide). The latter shape can more effectively accelerate ascending air parcels. Zipser (2003) offered another possible explanation: glaciation of water droplets when they are transported to the upper troposphere adds additional latent heat to

the air parcels, reinvigorating the convection. Land convection with higher aerosol concentration tends to delay warm rain and transports more water droplets to the higher levels where they glaciate.

Correlation coefficients between various parameters used to characterize convective properties are summarized in Table 2. A few results deserve discussion. 1) Relatively high correlation (0.78) is seen between CTH and LNB, suggesting that the vertical development of OSC tends to scale with LNB. Correlation coefficient is higher over ocean (0.83) than over land (0.70). 2) CTH and ETH (both 0 dBZ and 10 dBZ) are also positively correlated, although the correlation coefficients are smaller than that between CTH and LNB. This suggests that convective strength (as indicated by ETH) and cloud depth (CTH) are closely related. But unlike CTH and LNB, larger correlations between CTH and ETH are found over land than over ocean. This could be explained through the land-ocean contrast in convective intensity, namely, stronger convection over land dictates closer coupling between convective strength (indicated by ETH) and vertical development (indicated by CTH), whereas sluggish convection over ocean is loosely coordinated in the vertical. 3) LNB and ETH are also positively correlated, but the correlation coefficients are generally lower than those for LNB and CTH and for CTH and ETH. Recall that LNB can be thought of as an environmental parameter that caps deep convective development (Takahashi and Luo 2012). Our results suggest that this "capping" effect is stronger for CTH than for ETH. 4) Another parameter CloudSat provides is the OSD, which presumably also measures convective intensity but from a different perspective than ETH. Table 2 shows that the correlation between OSD and ETH are relatively small. It is not immediately clear to us why they are not well correlated. One possible reason may have to do with our analysis approach: CTH, ETH and OSD are recorded profile by profile (1.7 km along track and 1.3 km across track)

and the correlation coefficients are also calculated based on this profile-by-profile collection of measurements. Because of this, vertical wind sheer may displace OSD maximum from ETH maximum by more than the distance of 1.7 km so that it may "ruin" the one-to-one correlation. Nevertheless, when averaged over large regions for many OSC events, OSD and ETH tend to give consistent depiction of convective intensity.

3.3.3. Life stages of OSC

A unique aspect of this OSC study is the combination of CloudSat with geostationary satellite data. That is, each snapshot of OSC by CloudSat is cast in the context of the whole life cycle of the convective system (CS) in which it is embedded. Using size (R) and the minimum Tb of the CS from the ISCCP-CT database, we define three convective life stages: growing, mature and dissipating as described in Section 2.4.

We first investigate the question at which life stage(s) of the systems are the OSC events observed. We find that 2,300 cases of OSC events embedded at the growing stage of the CSs, 523 cases at the mature stages and 20 cases at the dissipating stages. However, the lifetime duration of each stage is different: the ratio of lifetime duration at growing, mature and dissipating stage is 0.35, 0.16, and 0.49, respectively. To avoid sampling bias among each stage, we normalize the results by dividing the total number of OSC events embedded in each life stage by the lifetime duration of that stage. This way, samples from the mature stage will get some "compensation" for fairness consideration because the mature stage is shorter than the other two stages, according to ISCCP CT data. After this adjustment, our result shows that OSC occurs predominately during the growing stage of the CSs (~ 66.2 % of all OSC cases); the mature stage comes second (~33.4 %) and only very few OSC cases (~ 0.4 %) are found during the dissipating

stage (Table 3). An interesting result is that about 1/3 of OSC is found at the mature stage of the CSs, because this suggests that although the convective systems start to detrain and develop anvils, many of them still experience strong updrafts that push cloud tops above the LNB. The dissipating stage is the period of decaying during which cloud tops get warmer (CTH starts decreasing) with time and size becomes smaller, thus OSC can hardly occur at this stage.

We also break down the statistics by land and ocean and by daytime (13:30) and nighttime (1:30) overpasses (Table 3). Occurrence frequencies of OSC embedded in each life stage over ocean appear to show little variation between daytime and nighttime. In other words, little diurnal variation is observed over ocean. Over land, OSC is less concentrated at the growing stage during the daytime than the nighttime; the mature stage has more share of OSC during the day than during the night. This can be interpreted as related to the diurnal cycle of convective intensity: stronger land convection in the afternoon time may sustain OSC plumes well into the mature stage of the convective system.

It is also of interest to examine the characters of the convective systems in which OSC events are embedded. Figure 3.6 shows the statistics of the system lifetime, max R, and the min TB (max R and min TB are used to define life stages; see Fig. 4). Maximum R is slightly larger over land than over ocean (but statistically insignificant at 95% confidence level). There are some larger differences in the distribution of lifetime and min TB between oceanic and continental convection (both statistically significant at 95% confidence level). Oceanic convection has longer lifetimes than continental convection: the mean and median for the ocean cases are, respectively 75.3 hr and 34 hr, while the values for land cases are, respectively, 47.2 hr 25 hr. Continental convection tends to have colder min TB (mean and median are both at 192 K) than oceanic convection (mean and median are both at 196 K).

Finally, we analyze convective strengths of the OSC embedded in different life stages of the convective systems (Table 4). Since OSC is rarely found in the dissipating stage (only 0.4% of all cases) and as such no enough statistics can be compiled, we only compare the growing stage and the mature stage. Almost all proxies in Table 4 point to stronger convective intensity for OSC during the growing stage, that is, larger ETH (both 0 dBZ and 10 dBZ), larger OSD and smaller CTETD.

3.4. Summary and discussions

Tropical overshooting convection (OSC) plays a critical role in affecting the heat and moisture budgets of the upper troposphere and lower stratosphere. Understanding these important influences requires, in part, ways of observing the tropics-wide distribution of OSC as well as their properties and behaviors. A number of satellite-based studies have been conducted in the past using, for example, IR, passive microwave and precipitation radar measurements. This current study approaches the subject from a different angle, emphasizing 1) the new and unique observations from the CloudSat cloud-profiling radar (CPR), and 2) the synergy between CloudSat snapshots and the whole convective life cycle as provided by geostationary satellite observations. The latter information is provided by the ISCCP Convection tracking (CT) database based on 3-hourly pixel-level geostationary data that give the life stage information of the convective system in which OSC events are embedded. The principal findings are briefly summarized as follows.

1) The occurrence frequency of OSC based on CloudSat observations is approximately 0.46 % between 30°S and 30°N and 0.69 % between 15°S and 15°N. They are partitioned into 50.6% over land and 49.4% over ocean, broadly consistent with previous statistics using IR

measurements. When the criteria for selecting OSC becomes more stricter with requirements of not only cloud-top height but also strong convective intensity, the land-ocean partition tilts toward land dominance, consistent with previous studies using TRMM PR and passive microwave measurements.

2) Regional variations in tropical OSC are investigated. Two contrasting regions are tropical warm pool (TWP) and tropical Africa: while the former has more occurrences of deep convection (DC) in general, the latter has more OSC. Amazon region is abundant in both DC and OSC. Caution, however, should be exercised to interpret these results because of the fixed sampling time (~ 1:30 am/pm local time).

3) CloudSat CPR offers a unique view of the internal vertical structure of OSC, which have not been systematically documented before. We analyze various parameters that are used to characterize cloud vertical extent (CTH), convective intensity (ETH, OSD and CTETD), and convective environment (LNB). Among all the regions, tropical Africa shows the strongest convective intensity. Correlations between these various parameters are also computed, generally showing close relationship between convective environment, cloud vertical development and convective strength.

4) ISCCP CT data are analyzed to identify the life stage of the convective system (CS) in which OSC events are embedded. It was found that OSC occurs predominantly during the growing stage of the CSs (66.2%); the mature stage comes second (33.4%) and only very few OSC cases are found during the dissipating stage (0.4%). There is little variation in the statistics between daytime (13:30) and nighttime (1:30) overpasses for oceanic cases; for land cases, however, OSC is less concentrated at the growing stage during the daytime than the nighttime

(see Table 3). Convective intensity is compared between the growing and mature stages of the CSs: almost all proxies point to stronger OSC during the growing stage.

This paper builds upon previous works and continues to elucidate the properties and behaviors of tropical OSC. The novel aspect of the study is that the CloudSat depiction of OSC is cast in the dynamic context provided by the geostationary satellite observations. The life stage view of OSC has important implications for mechanistic studies of tropical OSC and its influence on heat and moisture budgets of the upper troposphere and lower stratosphere. For example, knowing that OSC events are found predominantly in the growing stage of the CSs, future observational (e.g., field campaign) and modeling studies should therefore focus on the early duration of the system. The finding of the land-ocean and day-night differences is also intriguing. More detailed studies should be planned to understand why the mature stage claims more share of the OSC event during the day than at night for the land CSs but not for oceanic counterparts.

Table 3.1. Median values of LNB, CTH, OSD, CTETD of OSC for the whole tropics, over ocean and land separately, and for different regions (see Fig. 5 for the definition of the regions). Numbers in the parentheses are the standard deviations. Unit [m]

Median (STD)	LNB	CTH	OSD	CTETD 0dBZ	CTETD 10dBZ
Ocean	13,085 (1,386)	14,591 (1,280)	1,199 (788)	2,398 (1,653)	4,797 (2,354)
Land	12,495 (1,446)	14,516 (1,299)	1,679 (1,073)	2,158 (1,545)	4,317 (2,243)
Africa	12,349 (1,481)	14,514 (1,310)	1,918 (1,127)	2,159 (1,502)	4,317 (2,126)
Amazon	12,723 (1,368)	14,580 (1,211)	1,439 (1,003)	2,158 (1,534)	4,556 (2,250)
TWP	13,657 (1,256)	15,169 (1,039)	1,200 (858)	2,638 (1,761)	5,276 (2,420)
E.P. ITCZ	12,747 (1,136)	14,235 (992)	1,439 (759)	2,398 (1,516)	4,557 (2,213)
Atlantic ITCZ	12,647 (1,021)	14,078 (943)	1,199 (689)	2,158 (1,471)	4,317 (2,162)

Table 3.2. Correlation coefficiencies between different cloud and convective properties.

	Whole Tropics	Land	Ocean
CTH vs LNB	0.78	0.70	0.83
CTH vs ETH 0 dBZ	0.66	0.73	0.63
CTH vs ETH 10 dBZ	0.47	0.56	0.43
LNB vs ETH 0 dBZ	0.52	0.53	0.53
LNB vs ETH 10 dBZ	0.35	0.40	0.35
OSD vs ETH 0 dBZ	0.12	0.16	0.08
OSD vs ETH 10 dBZ	0.11	0.12	0.08

Table 3.3. Normalized occurrence frequencies of OSC for the three stages.

		Ocean		Land	
	All Cases	Noon (13:30)	Midnight (1:30)	Noon (13:30)	Midnight (1:30)
Growing	66.2%	74.1 %	74.7 %	66.0 %	72.7 %
Mature	33.4%	25.8 %	24.9 %	33.5 %	26.6 %
Dissipating	0.4%	0.1 %	0.4 %	0.4 %	0.7 %

Table 3.4. Median values of ETH, OSD, and CTETD for the OSC events enbeded in the growing and mature stagese of the CSs. Numbers in the parentheses are the standard deviations. Unit [m]

Median (STD)	Ocean/Land	ETH 0 dBZ	ETH 10 dBZ	OSD	CTETD 0 dBZ	CTETD 10 dBZ
Growing	Ocean	12,075 (1,987)	9,448 (2,296)	1,114 (523)	2,533 (1,471)	5,036 (1,983)
	Land	12,143 (2,051)	9,747 (2,219)	1,558 (919)	2,222 (1,285)	4,653 (1,880)
Mature	Ocean	11,200 (2,044)	8,903 (2,465)	1,106 (585)	2,744 (1,512)	5,120 (2,103)
	Land	11,602 (2,210)	9,470 (2,415)	1,559 (832)	2,278 (1,473)	4,588 (1,842)

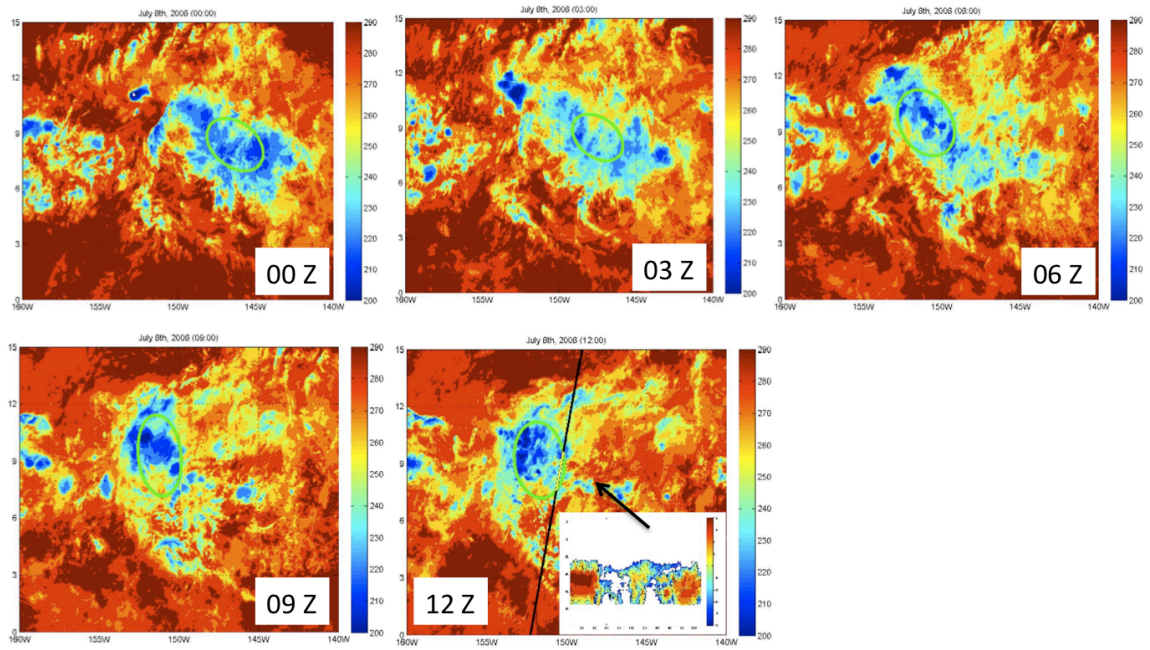

Figure 3.1. Evolution of a CS from 00 Z to 12 Z on July 6, 2006. Green ovals are the fitting ellipses which highlight the westward movement of the system. The black line on the lower right panel (12 Z) shows the CloudSat footprint and the inlet shows the CloudSat vertical cross section of the CS.

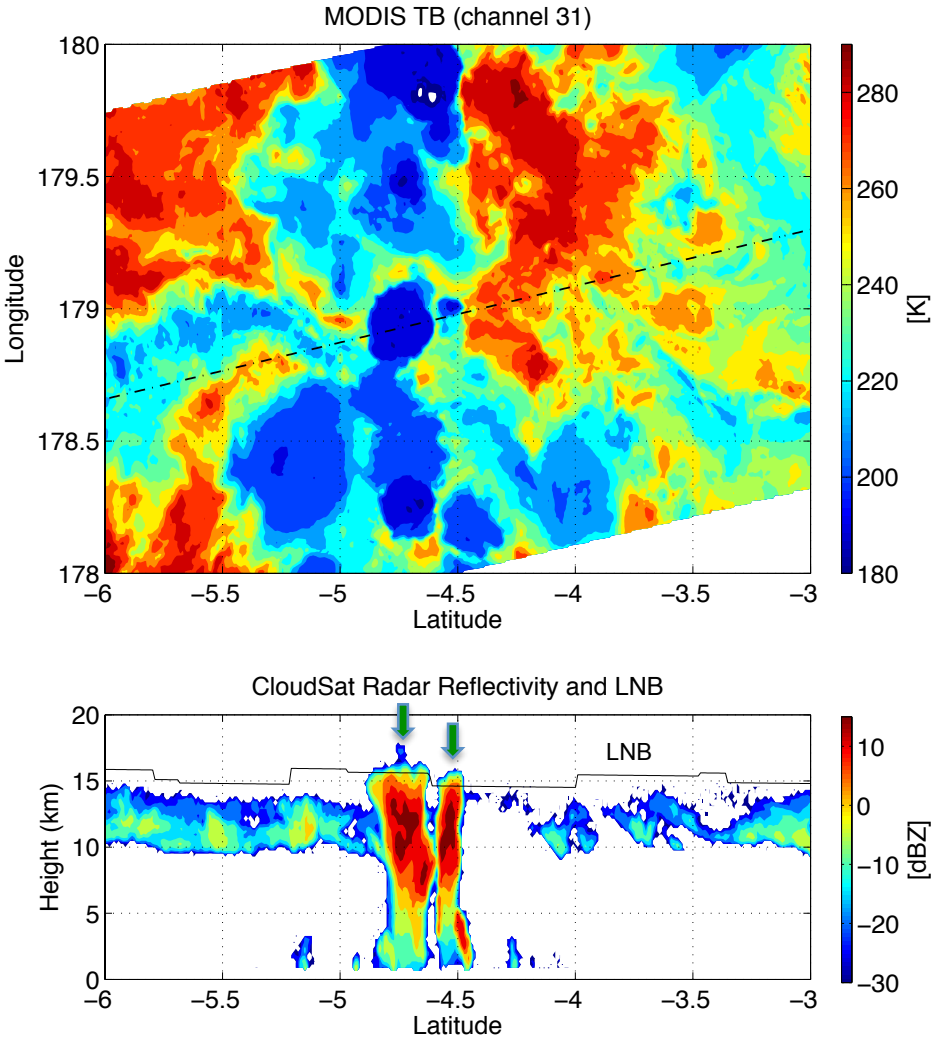

Figure 3.2. Example of overshooting features from different satellite view. MODIS (top) provides the plan view of the brightness temperature (a proxy of cloud top temperature), while CloudSat (bottom) provides vertical distribution of radar refractivity and cloud properties. The dotted line (top) indicates that CloudSat footprint. The black line (bottom) is the height of LNB, and the arrows point to the locations of the selected OSC.

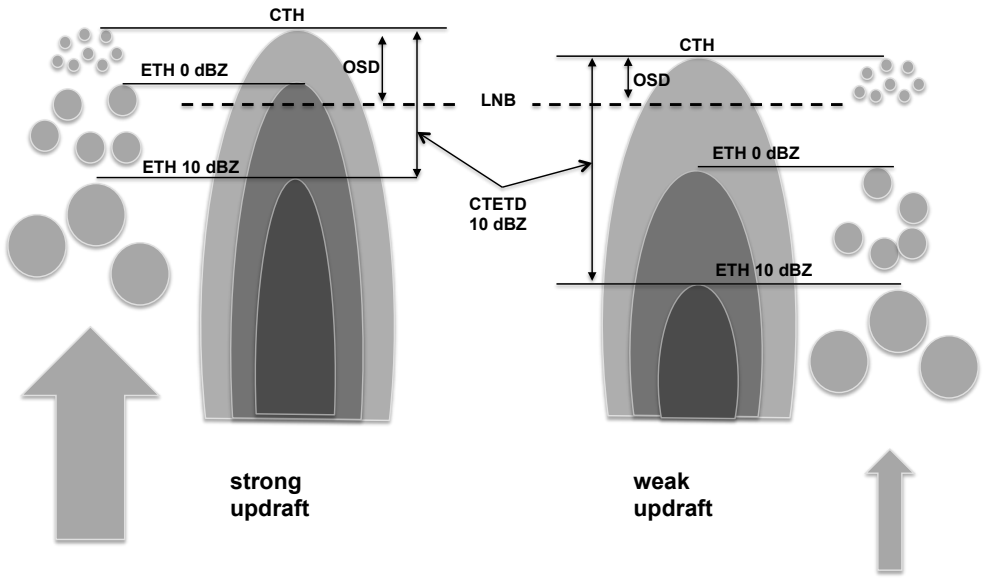

Figure 3.3. Schematics showing the three proxies of convective strength (ETH, OSD, and CTETD) for strong and weak updrafts.

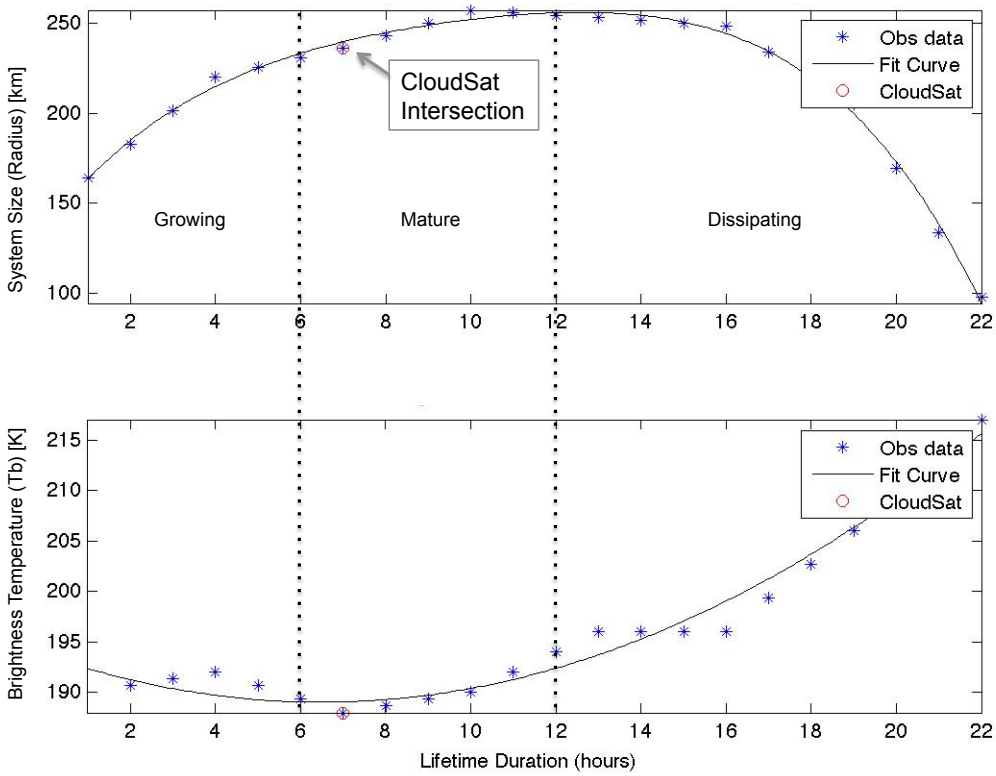

Figure 3.4. An example of the "growing stage", "mature stage", and "dissipating stage" classified by system radius and minimum brightness temperature. The curve shows the best fitting based on a F-test.

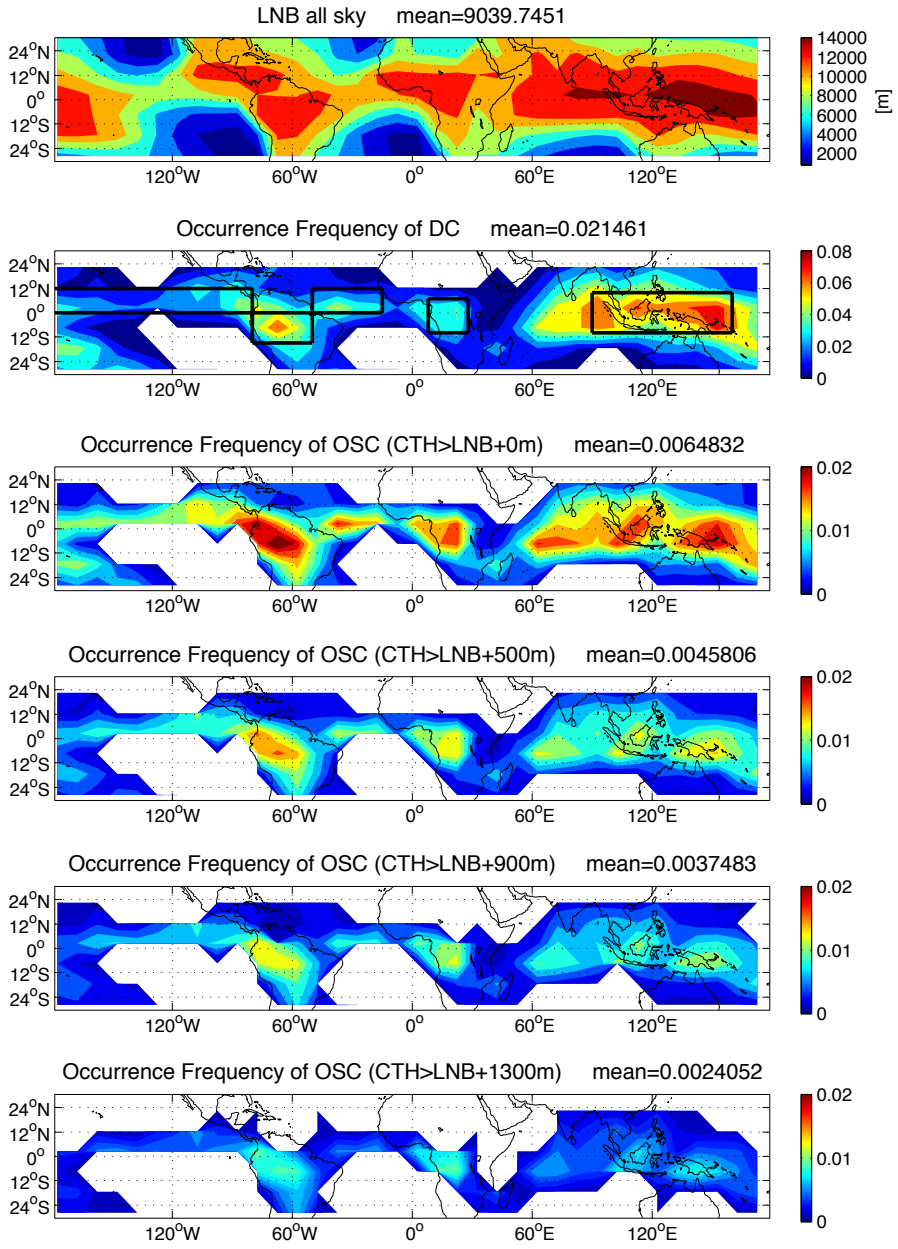

Figure 3.5. From the top to bottom: LNB (unit: m), occurrence frequency of DC, and occurrence frequencies of OSC with different δ values (from 0 to 1300m). Values are the means within each 10°× 10° grid box. Black solid boxes in the second panel are the five selected regions discussed in the text: tropical Africa, Amazon, tropical warm pool (TWP), eastern Pacific Intertropical Convergence Zone (E.P. ITCZ), and Atlantic ITCZ.

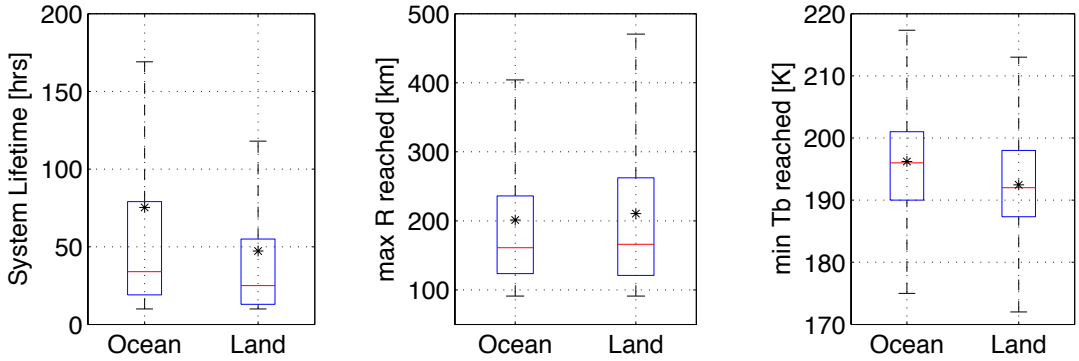

Figure 3.6. Box diagram for the system lifetime (left), peak system sizes reached (middle), and the minimum brightness temperature reached (right). The bottom and top of the boxes show, respectively, the 25% and 75% percentile. The central lines show the median and stars inside the box show the mean.

Chapter 4

Vertical Distribution of Water Vapor During EP- and CP-El Niños

The content of this chapter is conditionally accepted by *J. Geophys. Res.*

4.1. Introduction

El Niño–Southern Oscillation (ENSO) is characterized by anomalous sea surface temperature (SST) in the eastern-to-central equatorial Pacific. It plays an important role in interannual variability of global climate through strong teleconnection. Since a new type of El Niño named the Central Pacific (CP) El Niño or El Niño *Modoki* was discovered, much effort has been made to examine the mechanism of CP El Niño, which exhibits a unique horseshoe warming pattern in the equatorial central Pacific extending toward the subtropics (Ashok et al., 2007; Kao and Yu, 2009). A number of papers have pointed out that the impacts of this new type of El Niño over many parts of the globe are different from those of the canonical Eastern Pacific (EP) El Niño (Latif et al., 1997; Ashok et al., 2007; Kao and Yu, 2009; Kug et al., 2009; Weng et al., 2007; Weng et al., 2009; Kim et al., 2009). Furthermore, Kao and Yu (2009) emphasized that the EP El Niño is a cyclic oscillation coupled with basin-wide thermocline and surface wind variations and has strong teleconnection with the tropical Indian Ocean, while the CP El Niño is an event associated with atmospheric forcing rather than changes in thermocline and has stronger teleconnection with the Southern Indian Ocean.

The variations of cloudiness and cloud radiative forcing (CRF) during ENSO have been examined extensively (Ramanathan and Collins, 1991; Zhang et al., 1996; Cess et al., 2001; Allan et al., 2002). A recent study by Su and Jiang (2013) (hereinafter referred to as SJ13)

showed that the variations of tropical cloud vertical structure, CRF, and circulation during the 2006-07 El Niño (moderate EP El Niño) are strikingly different from those of the 2009-10 El Niño (strong CP El Niño). In terms of the tropical mean, for example, during the 2006-07 El Niño, the intensity of tropical circulation (primarily the Walker circulation) becomes weaker, with the amount of mid-high (low) clouds increases (decreases), and a net cloud warming effect (0.2-0.5 W/m^2) is found. On the contrary, during the 2009-10 El Niño, the intensity of tropical circulation (primarily the Hadley circulation) becomes stronger, with the amount of mid-high (low) clouds decreases (increases), and a net cloud cooling effect (0.6-0.7 W/m^2) is found. Moreover, SJ13 found that the variations of clouds and circulation during the two El Niños are more dominated by the magnitude than the pattern of anomalous SST. To further identify the different characteristics of the two types of El Niños, it is of interest to investigate variations in water vapor associated with the two ENSO events.

Water vapor is an important component of the atmosphere. It is a highly variable trace constituent of the atmosphere; it is also the primary contributor to the atmospheric greenhouse effect (Manabe and Wetherald, 1967). When water vapor condenses, a warming occurs due to the release of latent heat. In deep convection, the warm air parcel rises and develops into large cumulonimbus clouds, and then detrains at the upper troposphere. As such, water vapor plays an important role in energy balance and subsequently affects atmospheric circulation. As the CP El Niño has been more frequent than the EP El Niño since the 1980s (Latif et al., 1997; Ashok et al., 2007; Kao and Yu, 2009; SJ13), it is useful to document how the atmospheric moisture changes during the CP El Niño differ from those during the EP El Niño. The primary purpose of this paper is to reveal the variations of the vertical distributions of water vapor and its relation to clouds during the two different types of El Niño events. The data used are water vapor profiles

from the Atmospheric Infrared Sounder (AIRS) for the lower-to-middle troposphere (LT/MT) and from the Microwave Limb Sounder (MLS) for the upper troposphere to lower stratosphere (UT/LS). In parallel to SJ13, vertical distributions of water vapor in meridional and zonal planes during the 2006-07 and 2009-10 El Niños are analyzed first. Next, using the conditional sampling approach as in Bony et al. (2004), we examine how water vapor variations are connected to changes in large-scale circulation. We also compare the water vapor variations with those of clouds represented by CloudSat/CALIPSO cloud fraction (CFr) anomalies and CloudSat cloud water content (CWC) anomalies shown in SJ13.

Moreover, Geophysical Fluid Dynamics Laboratory (GFDL) AM2.1 model simulations of water vapor and clouds are examined and compared with the satellite observations. We evaluate how realistically the two El Niño events are simulated in the model and diagnose the discrepancies between the model simulation and the observations. The vertical structures of water vapor and clouds are important for radiation balance and thus climate. Climate models' skills in simulating the vertical structure of clouds and water vapor are far from satisfactory (Jiang et al., 2012; Su et al., 2013; Tian et al., 2013), while the model simulated interannual anomalies of water vapor and clouds have not been rigorously tested. At the time of the analysis, only GFDL AM2.1 was available to us to conduct a multi-year simulation driven by the observed SST that included the 2006-07 and 2009-10 El Niños. The comparison of model results with the observations helps to identify model weaknesses and guide future model improvements. Our diagnosis of model errors helps to identify the sensitive geographical regions for the tropical-mean interannual anomalies and the important teleconnection processes that determine the tropical-mean water vapor response during El Niños.

Finally, we regress the water vapor anomalies at each pressure level onto the Niño-3.4 SST (5°S -5°N and 190 - 240°E) using the data over the entire observational period of Aqua and Aura to extract the general features of water vapor response to ENSO SST forcing (focusing on the vertical variation of water vapor anomalies), and to quantify the average magnitude of water vapor response to the SST warming. In this paper, we focus on the ENSO responses over tropical ocean. The interannual anomalies over land are deferred to the future.

The rest of the paper is organized as follows. Section 4.2 describes the analysis methods and data used. Results and interpretations are presented in Section 4.3. Section 4.4 summarizes the study.

4.2. Data and analysis methods

AIRS on Aqua was launched in 2002, which carries a nadir-scanning sounder together with infrared and microwave retrievals (Aumann et al., 2003). It has 2378 IR channels in the spectral range from 3.74 to 15.4 μm and its footprint is approximately 13.5 km at nadir. The AIRS provides rich and accurate information about the atmosphere (water vapor, temperature, and minor gases such as CO_2, CO, CH_4, O_3, and SO_2) with the purpose of improving weather forecasting and studying water and energy cycle (Le Marshall et al., 2005). Chahine et al. (2006) provide a detailed overview of the AIRS data. We use AIRS version 5, Level 3 water vapor product AIRX3STD (Olsen et al., 2007) whose spatial resolution is 50 km, but aggregated on 1°×1° (longitude × latitude) grids. The estimated water vapor uncertainly is 25% in the tropics and the usable altitude range over the ocean is from 1000 hPa to 300 hPa (Jiang et al., 2012).

MLS on Aura was launched in 2004, designed to observe chemical constituents from the UT/LS by thermal emission from the atmospheric limb centered near 118, 190, 240, and 640

GHz, and 2.5 THz (Waters et al., 2006). It produces vertical profiles of atmospheric water vapor, temperature, cloud ice, and chemical tracers such as CO and O_3, etc. Its retrievals are horizontally spaced by 167 km along the orbital track (Waters et al., 2006), and the detailed retrieval methodology is described in Livesey et al. (2006). We use MLS Version 3, Level 2 water vapor product (Livesey et al. 2011). The vertical resolutions of the MLS water vapor are ~3.0 km, with 20% uncertainties at 215 hPa and 10% at 100 hPa. (Read et al. 2007; Jiang et al. 2010). To ensure best quality of data, we use the water vapor from AIRS at and below the 300 hPa pressure level and water vapor from MLS above the altitude of 300 hPa. For combined AIRS and MLS water vapor profiles, we use the data from 2004 to 2011, including 7 DJFs.

For cloud profiles, the CloudSat radar and Cloud-Aerosol Lidar and Infrared Pathfinder Satellite Observations (CALIPSO; Winker et al. 2003) combined CFr from 2B-GEOPROF-LIDAR are used together with the CWC produced by SJ13 from CloudSat Level 2BCWC-RO. The CloudSat and CALIPSO were launched in April 2006 (Stephens et al. 2008). The former satellite carries a 94-GHz cloud profiling radar (CPR; Im et al. 2006) that is sensitive to both cloud-size and precipitation-size particles and the latter is sensitive to optically thin clouds, which CPR might not capture. Combined CloudSat and CALIPSO measurements thus offer effective global survey of cloud vertical profile from deep convection to thin high clouds. The footprint of these data is 1.7 km along track and 1.3 km cross track, and the vertical resolution is 480 m (Stephens et al., 2002).

Aqua, Aura, CALIPSO and CloudSat are all members of the A-Train constellation (L'Ecuyer and Jiang, 2010), flying in a sun-synchronous orbit with an equator crossing time around 1:30 am/pm. Aqua leads Aura by about 8 minutes (Stephens et al., 2002). CALIPSO follows Aqua by 1-2 minutes and CloudSat by 10-15 seconds (Sun-Mack et al., 2007).

Following the satellite data analysis, we examine the simulated water vapor responses to the two El Niños in the GFDL AM2.1 model driven by the observed SST from 2005 to 2012. GFDL AM2.1 is an atmosphere-only model. It has high skills in reproducing dynamical response to tropical SST variability (including ENSO) (Lau et al. 2006) and consistently ranked among the top models with regard to the skills in simulating tropical variability (Annamalai et al. 2007). Su et al. (2011) evaluated the cloud simulations in one version of AM2 for the period of October 2006 to September 2007 using CloudSat data. However, the AM2.1 performance for the vertical structures of water vapor and clouds during the two recent El Niños has not been examined. The horizontal resolution is 2.5°×2° (longitude × latitude). It has 24 vertical levels: the lowest level is about 30 m above the surface, nine full levels are in the lowest 1.5 km above the surface, and five levels are in the stratosphere with the highest level at about 3 hPa (Anderson et al., 2004). This model uses 3 hourly intervals for atmospheric radiation and 0.5 hourly intervals for other atmospheric physics. A diurnal cycle of insolation is included in this model (Delworth et al., 2006). The model has a moist bias in the upper tropospheric relative humidity compare to Television and Infrared Observation Satellite (TIROS) Operational Vertical Sounder (Anderson et al., 2004).

As water vapor distribution strongly depends on temperature and altitude (it decreases by four orders of magnitude from the surface to the tropical tropopause), we mainly use water vapor fractional change (%), that is, the ratio of the change in specific humidity to the layer-averaged specific humidity, rather than changes in actual water vapor amounts (ppmv). Also, as El Niño warming is generally maximized in boreal winter, we focus on analyzing the water vapor anomalies averaged for December, January, and February (DJF). We use the methodology introduced by Bony et al. (2004) to understand the linkage between the water vapor distribution

and large-scale circulation. Fundamentally, water vapor and convection are controlled by thermodynamics (e.g., Clausius-Clapeyron (CC) relationship) and dynamics (e.g., rising or sinking motion), respectively. From a large-scale perspective, both dynamics and thermodynamics play an important role in affecting clouds and water vapor (Bony et al., 2004). In this framework, ω_{500}, mid-tropospheric vertical pressure velocity at 500 hPa, is used as a proxy of local dynamic condition, and water vapor is treated as a function of ω_{500} weighted by the probability density function of each ω_{500} regime. We use the following equation:

$$\delta(Q_\omega P_\omega) = Q_\omega \cdot \delta P_\omega + P_\omega \cdot \delta Q_\omega + \delta Q_\omega \cdot \delta P_\omega$$

where Q_ω is the water vapor in a regime of the value ω and P_ω is the probability distribution function of the regime ω. We use ω_{500} from the European Centre for Medium-Range Weather Forecasts (ECMWF) ERA-interim reanalysis dataset and define 20 bins of ω_{500} with the bin interval of 10 hPa/day. In such a framework, anomalies of water vapor ($\delta(Q_\omega P_\omega)$) can be decomposed into a dynamic component ($Q_\omega \cdot \delta P_\omega$), a thermodynamic component ($P_\omega \cdot \delta Q_\omega$), and co-variation between the two ($\delta Q_\omega \cdot \delta P_\omega$). Note that δQ_ω and δP_ω are anomalies from their climatological means.

4.3. Results

4.3.1. Comparison between the 2006-07 and 2009-10 El Niños

4.3.1.1. Tropical-mean anomalies of water vapor

Figure 4.1a shows the tropical-mean (30°S-30°N) water vapor fractional change for the two El Niños from the surface to 100 hPa with the error bars centered at zero, indicating the interannual fluctuations. In terms of tropical mean, both El Niños strongly hydrate the upper troposphere around 200 hPa level (by ~10%) and slightly dehydrate around

700 hPa level. The moistening around 200 hPa exceeds one standard deviation during the 2009-10 El Niño, close to 0.09. We call it "upper tropospheric amplification" of water vapor response to the SST warming. Considering the greenhouse effect of water vapor is mostly sensitive to the upper tropospheric water vapor (Soden et al., 1995), the amplified UT water vapor response to SST warming further underscores the importance of UT water vapor in global energy and water cycles. Earlier studies suggested that the upper tropospheric moistening is closely associated with deep convection (Betts, 1990; Sun and Lindzen, 1993; Su et al., 2006; Soden and Fu, 1995) and the variations of UT water vapor is positively correlated with SST (Su et al., 2006; Luo et al., 2012). However, a close examination of water vapor changes during the two El Niños reveal nonlinear relations between tropical-mean water vapor, convection (represented by clouds) and SST anomalies.

During the 2009-10 El Niño, water vapor anomalies are positive over most of the troposphere (Figure 4.1a) although both CWC and CFr anomalies at middle-to-upper troposphere (600 to 100 hPa) are negative (Figures 4.1b and c). The 2006-07 El Niño, on the contrary, experienced the same sign of water vapor and cloud anomalies throughout the troposphere. Obviously, the tropical-mean water vapor changes are not simply correlated with the amount of cloud changes. Furthermore, the magnitudes of water vapor changes during the two El Niños are not proportional to the magnitude of SST anomalies, either. During the 2009-10 El Niño, the tropical-mean SST anomalies (0.23 °C) is about twice as high as that during the 2006-07 El Niño (0.12 °C), while their water vapor fractional changes do not differ by a factor of 2. Assuming tropical-mean relative humidity stays at the climatological mean value (this is the so-called "constant relative humidity" assumption) and tropospheric temperature changes following moist adiabats, the hypothetical water vapor fractional changes would look like Figure 4.1d, with the

water vapor anomaly differences between the two El Niños proportional to the their SST anomalies. The apparent discrepancy of Figure 4.1d from Figure 4.1a motivates us to explore the water vapor changes in a detailed 3-dimentional view as we discuss in the following sections. It also suggests that the "constant relative humidity" assumption does not hold on interannual time scales. Previous studies indicated that the variations in tropical or global mean relative humidity can have important effects on global hydrological cycles (e.g. Richter and Xie, 2008).

4.3.1.2. Zonal and meridional structures of water vapor anomalies

Figures 4.2 and 4.3 display the meridional-mean (10°S-10°N) and zonal-mean (0-360°E) of water vapor anomalies (in color shadings) over ocean, respectively, together with anomalies of CFr (in contours). In both figures, the left panels show the results from satellite observations, and the right panels show the model simulations.

On the longitude-height cross-section, the 2006-07 El Niño (Figure 4.2a) produces moderately positive fractional changes of H2O over the western Indian Ocean (45 - 70°N) and the central Pacific (160 - 200°E), especially near the dateline. Over the eastern Indian (70 - 90°E) and the western Pacific (100 - 150°E) we see moderately negative moisture anomalies. In contrast, the 2009-10 El Niño (Figure 4.2b) has a widespread strong moistening across the central to eastern Pacific with a strong hydration near the dateline at 300-200 hPa. Strong negative anomalies are observed over the western Pacific and maritime continents, peaking at 400 hPa. Positive anomalies occur over the eastern Indian Ocean. For both El Niño events, the pattern of water vapor anomalies is similar to that of CFr; however, some differences are outstanding during the 2009-10 El Niño. First, the peak heights of both negative and positive water vapor anomalies are lower than those of CFr. Second, while water vapor has positive

anomalies over the eastern Indian, such positive anomalies are not observed in CFr. We have also compared the water vapor anomalies to CWC anomalies during the 2009-10 DJF and found that negative CWC anomalies are observed over most of the eastern Indian with a very narrow band of positive anomalies (SJ13). The balance between the moistening due to the evaporation of ice particles and the drying due to the detrainment from cold overshooting turrets is a subject that warrants further investigation.

During the 2006-07 El Niño, the difference between the satellite observation (Figure 4.2a) and GFDL model (Figure 4.2c) is outstanding in terms of amplitude. The modeled simulated alternating positive and negative moisture anomalies from the eastern Pacific (200° -270°E) to the western Indian Ocean (45-70E) are about two times stronger than the satellite observations. During 2009-10 El Niño, the differences between the modeled and observed water vapor anomalies are mainly over the eastern Indian Ocean (45-90E), where opposite signed anomalies are shown for the observation (Figure 4.2b) and the AM2.1 simulation (Figure 4.2d). In addition, the peak altitudes of CFr anomalies from the CloudSat/CALIPSO retrieval are much higher than the GFDL AM2.1 simulation for both El Niños, which could be mitigated by using CloudSat/CALYPSO simulator cloud fraction if available (Su et al., 2013). Despite of the deficiencies mentioned above, the GFDL AM2.1 captures the general pattern of water vapor responses to the ENSO SST forcing.

On the latitude-height cross-section, the differences in the positive water vapor anomalies between the two El Niños (Figures 4.3a and 4.3b) are not as distinctive as those in the negative anomalies. Except for the facts that anomalous moistening is slightly shifted toward the north of the equator during the 2006-07 El Niño but toward the south of the equator during the 2009-10 El Niño and that the boundary layer moistening is more pronounced during 2009-10 El Niño, the

moistening of the atmosphere in response to the two El Niño events are very similar. The peak heights of increasing water vapor are found around 200 hPa in both El Niño events, which are associated with cloud ice detrainment. In contrast, the differences of anomalous drying in response to the two El Niños are rather outstanding. First, the magnitude of drying anomalies over the northern hemisphere during the 2009-10 El Niño is much stronger than that during the 2006-07 El Niño, especially over the 7-20°N zone. Second, the anomalous drying is widely spread over 15-30°S during the 2009-10 El Niño, while a mixture of anomalous moistening and drying are found for the 2006-07 El Niño. These differences are consistent with the distribution of CWC anomalies, which exhibit a broadly strong positive anomaly to the north of the equator during the 2006-07 DJF but a narrowly distributed cloud enhancement to the south of the equator during the 2009-10 DJF (SJ13). Negative CWC anomalies are found on the both sides of anomalous ascent, but they cover relatively very small areas (5-10°S and 10-15°N) during the 2006-07 El Niño, compared to a much larger area (10-30°S and 5-30°N) during the 2009-2010 El Niño. However, the stronger drying over the northern than the southern hemisphere during the 2009-10 El Niño are not consistent with the negative CWC anomalies which show equally strong magnitudes over both hemispheres (SJ13), but are in line with the negative CFr anomalies. During the 2009-10 El Niño, the strength of the Hadley circulation increases (SJ13). The substantial drying over the northern hemisphere may be because the stronger Hadley Cell resides over the winter hemisphere, which produces anomalously strong sinking motion over the subtropics in the northern hemisphere. Water vapor and CFr anomalies appear to be more sensitive to the variation in the Hadley circulation than the CWC anomalies.

The zonal-mean water vapor anomalies are very different between the satellite observation (Figures 4.3a and 4.3b) and the GFDL AM2.1 simulation (Figures 4.3c and 4.3d). The difference

in the amplitude of negative anomalies is significant in the Northern Hemisphere, where AM2.1 simulated water vapor anomalies are much drier in the lower to middle troposphere than the satellite observation for the 2006-07 El Niño but reversely for the 2009-10 El Niño. The differences around the equator and in the Southern Hemisphere are also evident: during the 2006-07 El Niño, GFDL AM2.1 underestimates the moistening at the equator but overestimates it between 10S-20S; during the 2009-10 El Niño, AM2.1 overestimates the mid-tropospheric moistening around the equator but underestimates the lower tropospheric drying between 10N-20N and between 20S-30S. In addition, the observed "upper tropospheric amplification" of moistening at the equatorial zone is not simulated in the model. The lower altitudes of peak moistening could be related to the lower altitude of peak convective detrainment indicated by the maximum CFr anomalies. Moreover, AM2.1 strongly overestimates the amplitude of CFr anomalies, by a factor of 10 in some places. It might not be very fair to demand the model to reproduce the zonal mean cloud anomalies because the zonal mean anomalies result from the compensation of large regional anomalies (Figures 4.3c and 4.3d) and are one order of magnitude smaller than the regional anomalies such as those shown in Figure 4.2.

4.3.1.3. Water vapor anomalies sorted by large-scale circulation

Figure 4.4 shows the water vapor profiles and their anomalies sorted by the 20 bins of ω_{500} with a bin interval of 10 hPa/day for the two El Niños in the observations and in AM2.1 simulations. In general, water vapor at all levels increases monotonically with decreasing ω_{500} (except at the strongly descending regime, where the occurrence frequency is close to zero). The modeled 3-month (DJF) mean water vapor profiles appear to be moister than the observed at all vertical heights, but the variation of water vapor with ω_{500} is captured. Both the 2006-07 and

2009-10 El Niños have anomalous moistening over strongly ascending regimes (ω_{500} < -75 hPa/day). Over moderately descending regimes (20 < ω_{500} < 50 hPa/day), both the 2006-07 and 2009-10 El Niños have anomalous moistening above 300 hPa; however, the 2006-07 El Niño has anomalous drying and the 2009-10 El Niño has strong anomalous moistening below 300 hPa. In between these two regimes (-75 < ω_{500} < 20 hPa/day), the 2009-10 El Niño has strong drying anomalies, whereas the 2006-07 El Niño has a mixture of both moistening and drying anomalies. Overall, the pattern of water vapor anomalies is similar to that of CFr anomalies in contours, especially during the 2009-10 El Niño (Figure 4.4d). The exception is found during the 2006-07 El Niño over the strongly ascending regimes (ω_{500} < -75 hPa/day) where water vapor has positive anomalies, but CFr has negative anomalies (Figure 4.4c). In contrast to the similarity between the model simulations and the observations in terms of the seasonal mean water vapor profiles, the anomalies of water vapor in the ω_{500} regimes show large discrepancies from the observations. For the 2006-07 El Niño, the model overestimates the moistening and drying anomalies in the intermediate circulation regime (-50 < ω_{500} < 10 hPa/day). For the 2009-10 El Niño, the model simulates a broad anomalous moistening in this intermediate circulation regime, opposite to the observed anomaly.

Figure 4.5 shows the three components of the fractional water vapor anomalies as a function of large-scale circulation regimes (Figure 4.4c and 4.4d, hereafter referred to as the total anomalies): the dynamic component ($\sum(Q_\omega \delta P_\omega)$, a and b), thermodynamic component ($\sum(P_\omega \delta Q_\omega)$, c and d), and co-variation ($\sum(\delta Q_\omega \delta P_\omega)$, e and f), which is small compared to the first two components. The AM2.1 simulations are shown together with the observations.

Comparing the two El Niños, the differences in the dynamic component are more outstanding than in the thermodynamic component. The patterns of the thermodynamic

component for both El Niños display a ubiquitous moistening in the upper troposphere and some drying in the lower troposphere, with a peak around the maximum pdf (probability density function) of ω_{500} at 10-20 hPa/day. The stronger UT moistening in 2009-10 is consistent with its larger amplitude of SST warming. This confirms that the thermodynamic component is primarily controlled by SST anomalies. However, the distributions of the dynamic component for each El Niño are qualitatively different. In 2006-07, a complicated pattern of alternating positive and negative anomalies is shown (Figure 4.5a), while a clear "sandwiched" positive-negative-positive pattern is found (Figure 4.5b) in 2009-10 with much stronger amplitudes. The dynamic component is driven by the pdf change of $\omega_{500.}$ The patterns in Figure 4.5a and 4.5b are manifestation of the effects of large-scale circulation changes on the water vapor profiles. As elaborated in SJ13, the Hadley Circulation strengthens during the 2009-10 El Niño, producing increased moisture at the strongly ascending and descending regimes and decreased moisture at the intermediate regime. During 2006-07 El Niño, the Walker Circulation weakens. The pdf changes of ω_{500} yield an increase of moisture in the moderate circulation regimes accompanied by small-amplitude alternating anomalies in nearby circulation regimes. This dynamic component for 2006-07 is different from that in SJ13, because the climatological ω_{500} distribution is based on the 7 years (2004-2011) instead of the 4 years (2006-2010) in SJ13.

Table 4.1 shows the sum of the total anomalies and its three components over all vertical levels and over the tropical oceans for the two El Niños. During the 2006-07 El Niño, the thermodynamic component (0.46) far outweighs the dynamic component (0.047) on the tropical mean. The pattern of the total anomalies (Figure 4.4c) is also similar to the thermodynamic component (Figure 4.5c). The 2009-10 El Niño seems to draw a different story: although the thermodynamic component (0.65) is larger than dynamic component (-0.096) on the tropical

mean, the pattern of the total anomalies (Figure 4.4d) is similar to the pattern of the dynamic component (Figure 4.5b). These results suggest that the tropical-mean water vapor anomaly is mostly determined by the thermodynamic factor (e.g., the temperature control), while local water vapor anomalies are strongly influenced by the dynamic factor such as ascent or descent anomalies. During the 2006-07 El Niño, the large-scale circulation changes are of weaker magnitude (SJ13) than during the 2009-10 El Niño. Therefore, the water vapor anomalies are mostly controlled by the thermodynamic factor during the 2006-07 El Niño, but they are dependent on both dynamic and thermodynamic changes during the 2009-10 El Niño.

Examining the water vapor simulations in the large-scale circulation regimes reveals more clearly the differences between the satellite observations and model simulations. Despite the quantitative differences in the amplitude of moistening anomalies, the thermodynamic components simulated in AM2.1 are similar to the observed, because they are primarily driven by observed SST. On the other hand, the model simulated dynamic components deviate from the observations significantly for both El Niños. The model overestimates the dynamic changes in all circulation regimes for the 2006-07 El Niño. In the moderate ascending regime around -25 hPa/day of $\omega_{500,}$ the sign of anomaly is opposite to the observed. For the 2009-10 El Niño, the model simulated dynamic component is nearly a reversed "sandwich" compared to the observed. Our analysis suggests that the dynamic component associated with the interannual changes of large-scale circulation are difficult to simulate, while the temperature-driven thermodynamic component is relatively easy to reproduce as the model is driven by the observed SST.

On the tropical-mean, the fractional water vapor anomalies in the different circulation regimes shows anomalous moistening in both El Niños; however, anomalous drying is found from the AM2.1 model simulations, especially during 2009-10 El Niño (Table 4.1). During the

2006-07 El Niño, the model simulated dynamic component (-0.202) outweighs the thermodynamic component (-0.080), and the patterns of the total anomalies (Figure 4.4g) are similar to the dynamic component (Figure 4.5g), which is inconsistent with the satellite observation. The 2009-10 El Niño, on the other hand, the model simulated thermodynamic component (-1.194) outweighs the dynamic component (-0.036) and the patterns of the total anomalies are similar to the dynamic component (Figure 4.5h), which is consistent with the satellite observation but with a reversed sign of anomalies.

We analyze further the contribution of each ocean basin to the total anomalies and find that the discrepancy between the satellite observation and model simulation predominantly lies in the Indian Ocean. Figure 4.6 shows the same analysis applied to the Indian Ocean only. The model simulation shows nearly opposite anomalies in ascending regimes to the observation for both El Niño events. ENSO excites strong teleconnection into the tropical Indian Ocean where a basin-wide warming usually occurs during El Niño (Klein et al. 1999; Du et al. 2009). Thus, the Indian Ocean experiences local SST forcing and remote ENSO teleconnection. Atmospheric GCMs tend to respond excessively to local Indian Ocean SST anomalies (Kumar and Hoerling, 1998), leading to errors in tropical-mean cloud and water vapor anomalies. To understand why the model fails to reproduce the water vapor response over the Indian Ocean, sensitivity model experiments are needed and more El Niño events should be examined.

4.3.2. Regression analysis of water vapor anomalies on the Niño-3.4 SST

Since the two El Niños examined might not represent averaged water vapor response to the SST forcing, we expand the analysis to the 8-year AIRS/MLS water vapor over the entire overlapped Aqua/Aura period (2004-2011). Regression of water vapor mixing ratio anomalies

(Figure 4.7, Left) and relative humidity (RH) anomalies (Figure 4.7, Right) onto the Niño-3.4. SST (5°S -5°N and 190 - 240°E) is conducted. The vertical profiles of regression coefficients for the fractional water vapor (Figure 4.8, Left) and RH (Figure 4.8, Right) are further examined over the western Pacific (10°S -10°N and 100 - 150°E) and the central Pacific (10°S -10°N and 160 - 200°E) separately, where the most pronounced negative and positive cloud anomalies are observed, respectively, during the two ENSO events, together with those for the whole tropics (30°S -30°N).

The spatial maps (Figure 4.7) show that water vapor and Niño-3.4 SST are positively correlated over the central Pacific (except at 100 hPa) and negatively correlated to the northwest and southwest of the central Pacific, forming a "horse-shoe" pattern. Spatial distributions of regression for water vapor mixing ratio and RH are broadly similar in the LT/MT (900-215 hPa). However, they look very different at 100 hPa. This is because near the tropopause, water vapor and RH variations are highly controlled by temperature, which produces an opposite sign of anomaly compared to the levels below. From Figure 4.8, we can clearly see the "upper tropospheric amplification" of water vapor response to SST warming, which is consistent with the two particular El Niños, especially over the central Pacific. This confirms that although water vapor is more abundant at the surface, the tropical upper troposphere moistens up at a faster rate in the fractional sense than the surface during El Niños. Su et al. (2006) pointed out that the rate of UT water vapor increase with SST is about 3 times of that implied by the CC equation (7% /C). A previous study by Chuang et al. (2010) showed the fractional increase rate of water vapor with SST ($q^{-1}dq/dSST$) is ~0.18/C at 250 hPa when q is averaged over whole tropics and SST is averaged over convective regions by using AIRS data. Luo et al., (2012) analyzed MOZAIC (Measurement of Ozone and Water Vapor by Airbus In-Service Aircraft)

data and found that the $q^{-1}dq/dSST$ in the vicinity of deep convective outflow is ~0.16/C at 262 hPa and ~0.18/C at 238 hPa. The fractional increase rate of water vapor with Niño-3.4. SST ($q^{-1}dq/dSST3.4$) is the highest over the central Pacific around 200 hPa (0.28/C), which is much higher than those from Chuang et al. (2010) and Luo et al., (2012). On the other hand, the western Pacific experiences anomalous drying over most of the troposphere, which partially compensates the moistening in the central Pacific, leading to rather small changes in the tropical-mean water vapor (within one standard deviation of regression fitting), except in the UT. The tropical-mean relative humidity regression with Niño-3.4 SST is also insignificant with a relatively large amplitude in the UT.

4.4. Summary and discussion

This study examines the vertical distribution of water vapor anomalies during the two different types of El Niños, EP and CP El Niños, following the study of SJ13. SJ13 showed that tropical-mean cloud responses to the two El Niño are nearly opposite in terms of anomalous cloud vertical profiles and TOA (top of atmosphere) cloud radiative forcing. The large-scale circulation changes are also drastically different during the two El Niños (SJ13). In this study, we compare the vertical structures of water vapor anomalies during the two El Niños in both conventional geographical space and large-scale circulation regimes. We further decompose the water vapor anomalies into the dynamic and thermodynamic components to delineate the physical mechanisms that drive the water vapor changes. GFDL AM2.1 model simulations of water vapor and CFr are examined and compared with the satellite observations. Besides analyzing the two El Niños, we also conduct a regression analysis of the water vapor and relative humidity profiles onto the Niño-3.4 SST use the 8-year AIRS/MLS observations to obtain an

ensemble behavior of tropical water vapor response to El Niño SST warming. The principal findings are as follows:

1. In terms of tropical mean, both El Niños strongly hydrate upper troposphere around 200 hPa and slightly dry out around 700 hPa, and lower tropospheric (1000 to 800 hPa) moistening is observed only during the 2009-10 El Niño. Although both CFr and CWC in the middle-to-upper troposphere have negative anomalies during the 2009-10 El Niño, water vapor anomalies are positive from 600 to 100 hPa.
2. The tropical-mean water vapor anomalies are primarily controlled by the thermodynamic component (i.e., temperature anomalies), while local anomalies are governed by both the thermodynamic and dynamic components (i.e., circulation changes). The large-scale circulation changes have a strong influence on water vapor anomalies in the 2009-10 El Niño, but have a relatively weak role in the 2006-07 El Niño.
3. A clear "upper tropospheric amplification" of the fractional water vapor change to El Niño is found The rate of increase of water vapor with Niño-3.4 SST exceeds the CC value of 7%/C and is the highest around 200 hPa (28%/C) over the central Pacific where enhanced convection is observed. The tropical-mean relative humidity change is about 1%/C, within the one standard deviation.
4. In terms of zonal/meridional means, GFDL AM2.1 model simulates the general patterns of water vapor response to the ENSO SST forcing. However, GFDL AM2.1 does not reproduce the strong moistening effect at 200 hPa where convective detrainment preferably occurs. Instead, the model simulated maximum CFr anomalies are found between 300 to 700 hPa level, lower than the observed maximum detrainment level.

5. The model is able to reproduce the thermodynamic component of water vapor anomalies, but does not capture the dynamic component associated with large-scale circulation changes. A critical region that dominates the model errors is found to be the Indian Ocean where the model probably overestimates the response to local SST anomalies but underestimates the teleconnection influence on regional water vapor. To better understand this deficiency, further analysis and additional model sensitivity experiments are needed to understand the model performance and improve model simulations of ENSO responses.

Table 4.1. The sum over all vertical levels and over the tropical oceans for fractional water vapor (H_2O) anomalies in the different circulation regimes ($\delta(Q\omega P\omega)$) and the dynamic component ($Q\omega\delta P\omega$), thermodynamic component ($P\omega\delta Q\omega$), and co-variation ($\delta Q\omega\delta P\omega$) during 2006-07 and 2009-10 El Niños.

	Satellite Observation		**GFDL Model Simulation**	
Sum	2006-07 El Niño	2009-10 El Niño	2006-07 El Niño	2009-10 El Niño
$\delta(Q\omega P\omega)$	0.51	0.55	-0.26	-1.21
$Q\omega\delta P\omega$	0.047	-0.096	-0.202	-0.036
$P\omega\delta Q\omega$	0.46	0.65	-0.08	-1.194
$\delta Q\omega\delta P\omega$	0.0025	0.0020	-0.019	-0.02

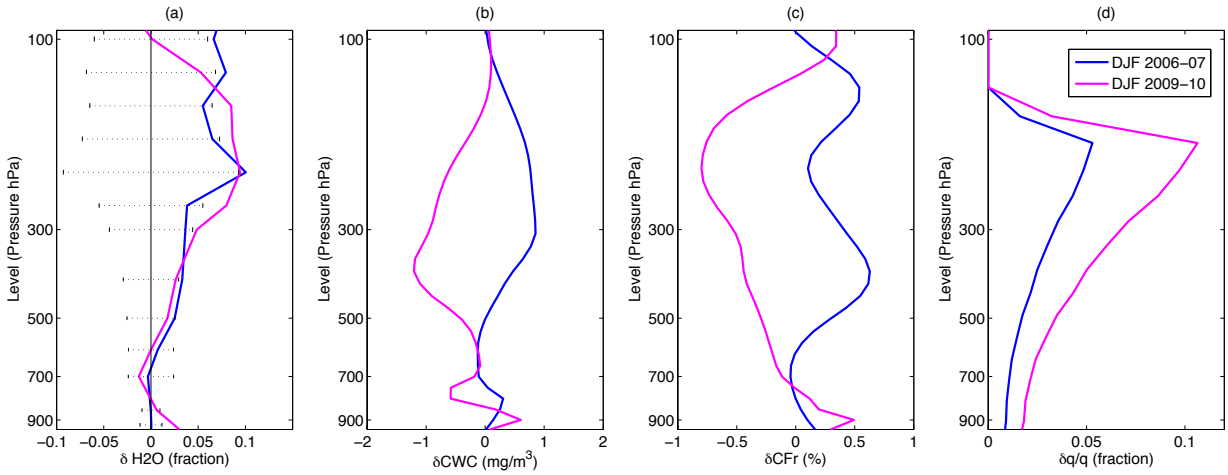

Figure 4.1. Tropical-mean (30°S-30°N) anomalies of water vapor fraction (a) with the error bars (std) centered at zero, cloud water content (b), cloud fraction(c), and hypothetical water vapor (H_2O) fraction changes under "constant relative humidity" assumption (see text for details) (d) for two El Niños at different pressure levels. Blue line represents during the 2006-07 El Niño and magenta line represents during the 2009-10 El Niño.

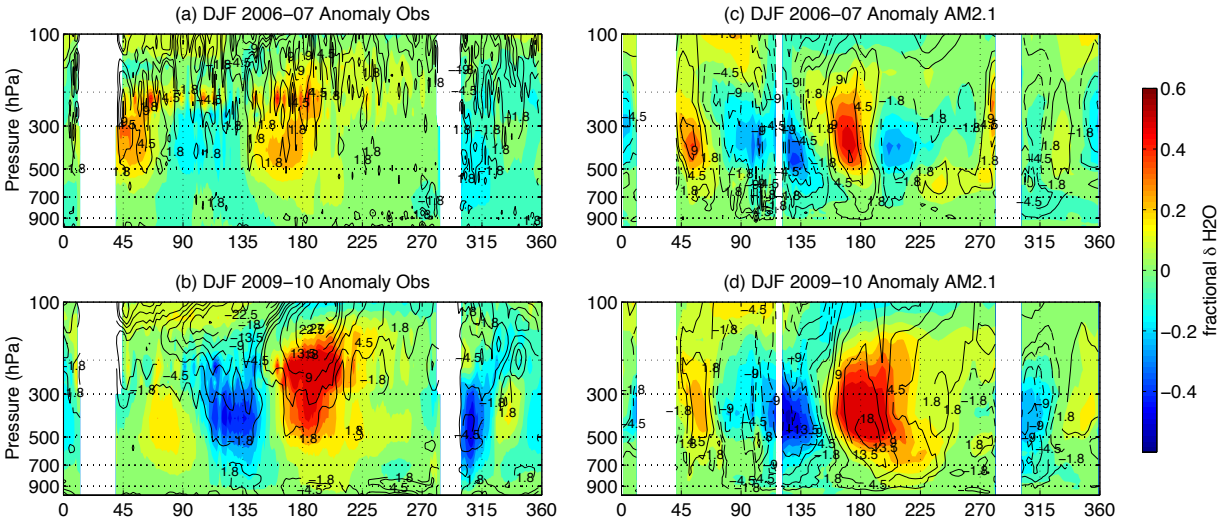

Figure 4.2. Longitude-height section of tropical-mean (10°S-10°N) anomalies during the DJF 2006-07 El Niño and the DJF 2009-10 El Niño from satellite observations (a, b) and model simulations (c, d). Shadings represent fractional water vapor (H_2O) and contours represent cloud fraction (CFr).

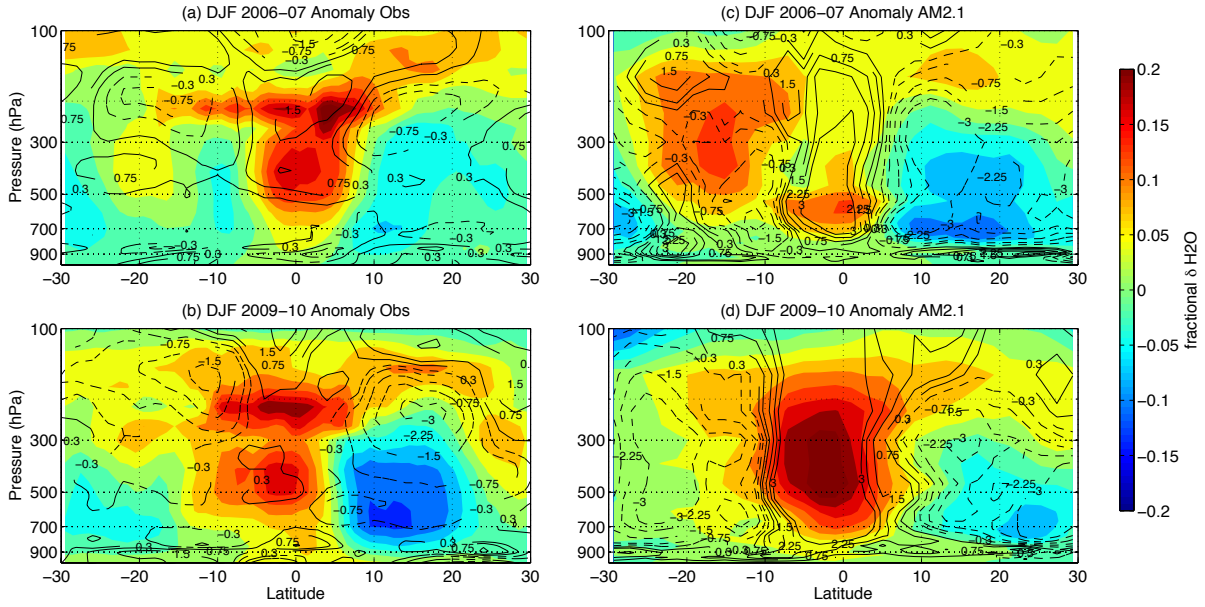

Figure 4.3. Latitude-height section of zonal mean (0-360°E) anomalies during the DJF 2006-07 El Niño and the DJF 2009-10 El Niño from satellite observations (a, b) and model simulations (c, d). Shadings represent fractional water vapor (H_2O) and contours represent cloud fraction (CFr).

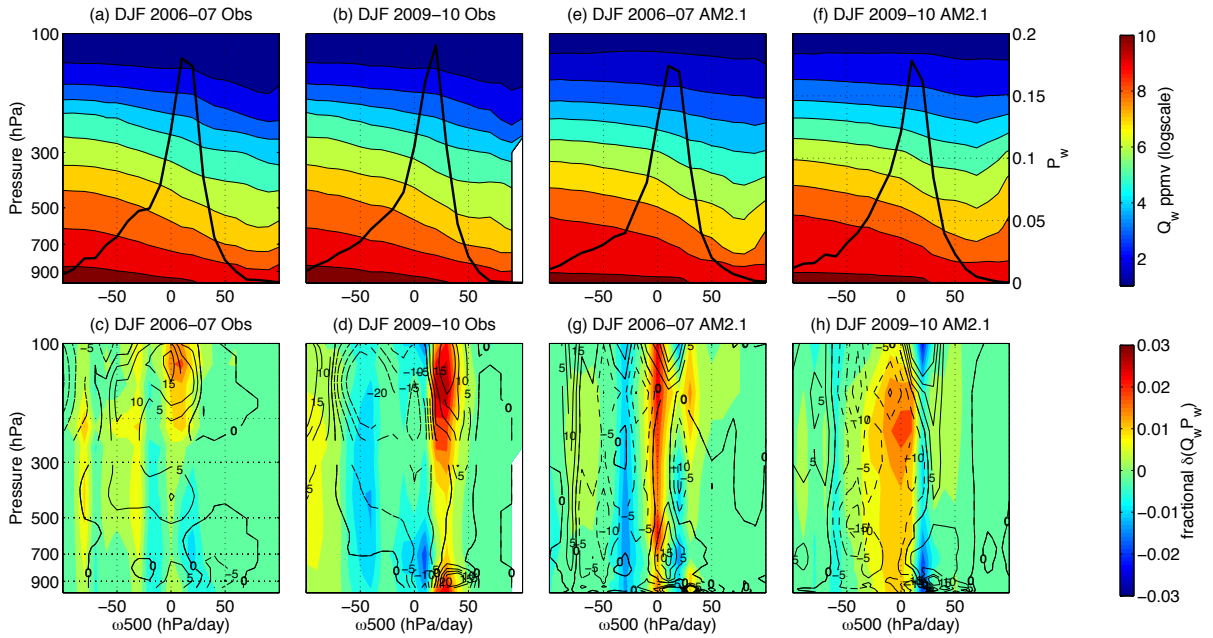

Figure 4.4. Water vapor sorted as a function of vertical pressure velocity at 500 hPa, ω_{500} (a, b, e, and f) and fractional water vapor (H_2O) anomalies as a function of ω_{500} weighted by probability density function of each regime (c, d, g, and h) during the DJF 2006-07 El Niño (left panel) and during the DJF 2009-10 El Niño (right panel). The solid curves in (a), (b), (e), and (f) are probability density function of each regime. Line contours in (c), (d), (g), and (h) represent cloud fraction (CFr) (unit: 10^{-3} %). (a)-(d) are from satellite observations and (e)-(h) are from model simulations.

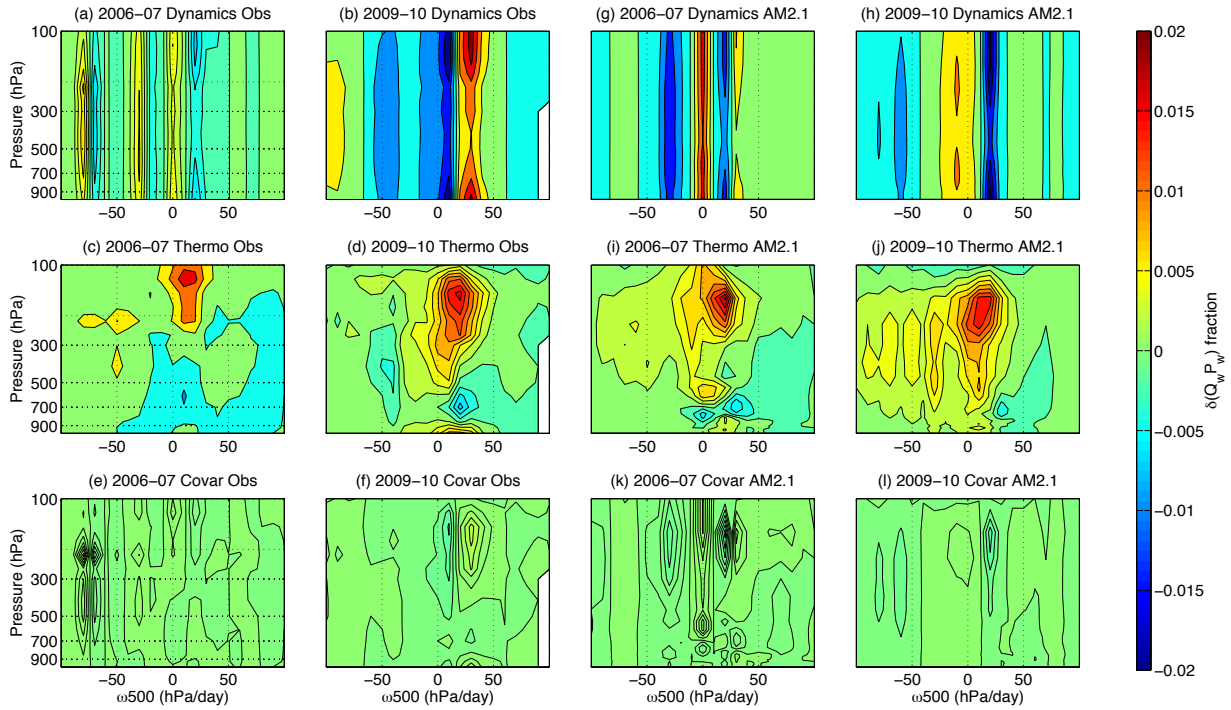

Figure 4.5. Three components, dynamic component (a, b, g, and h), thermodynamic component (c, d, i, and j), and co-variation (e, f, k, and l), of fractional water vapor anomalies changes as a function of ω_{500} during the DJF 2006-07 El Niño and during the DJF 2009-10 El Niño. (a)-(f) are from satellite observations and (g)-(l) are from model simulations.

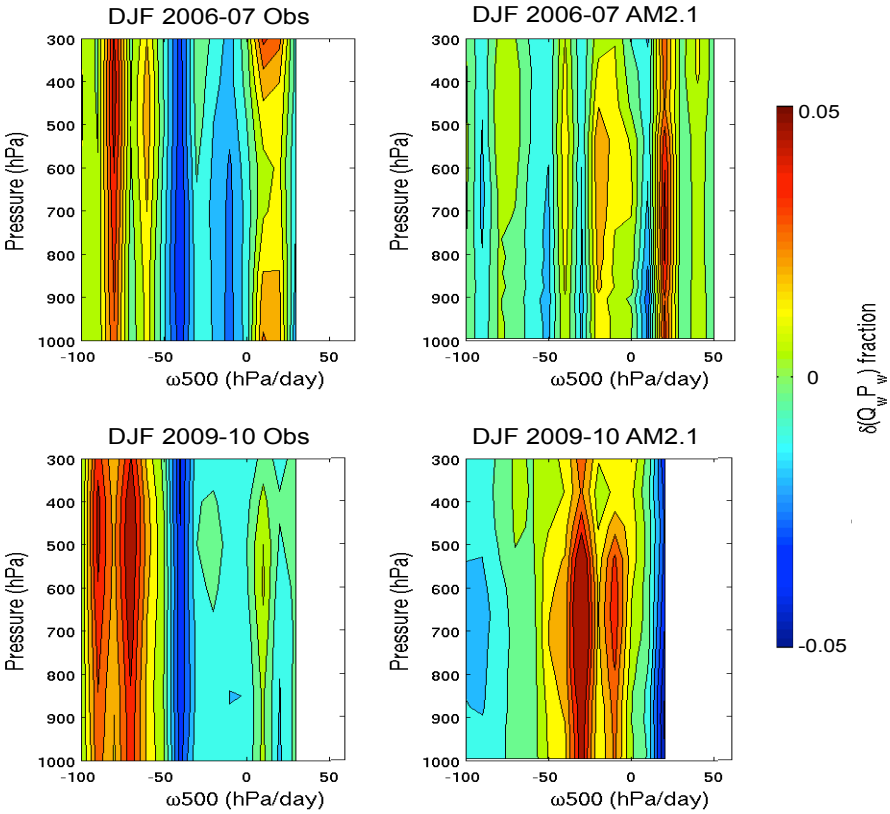

Figure 4.6. Same as Figures 4c and 4d (left panel) and Figures 6c and 6d (right panel) but limited the region over the Indian Ocean.

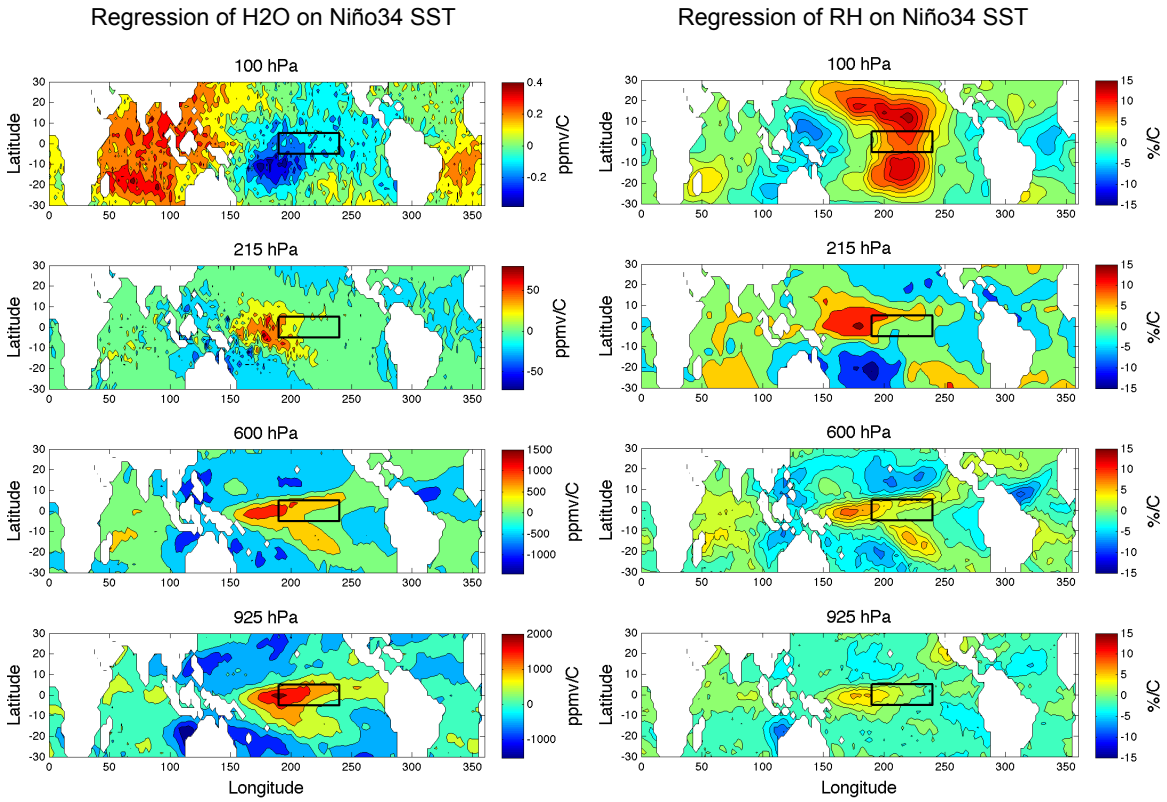

Figure 4.7. Regressions of water vapor mixing ratio anomalies [ppmv/C] (left panel) and relative humidity anomalies [%/C] (right panel) onto the Niño-3.4 SST at four vertical levels. Black box is the area of Niño-3.4. SST (5°S -5°N and 190 - 240°E).

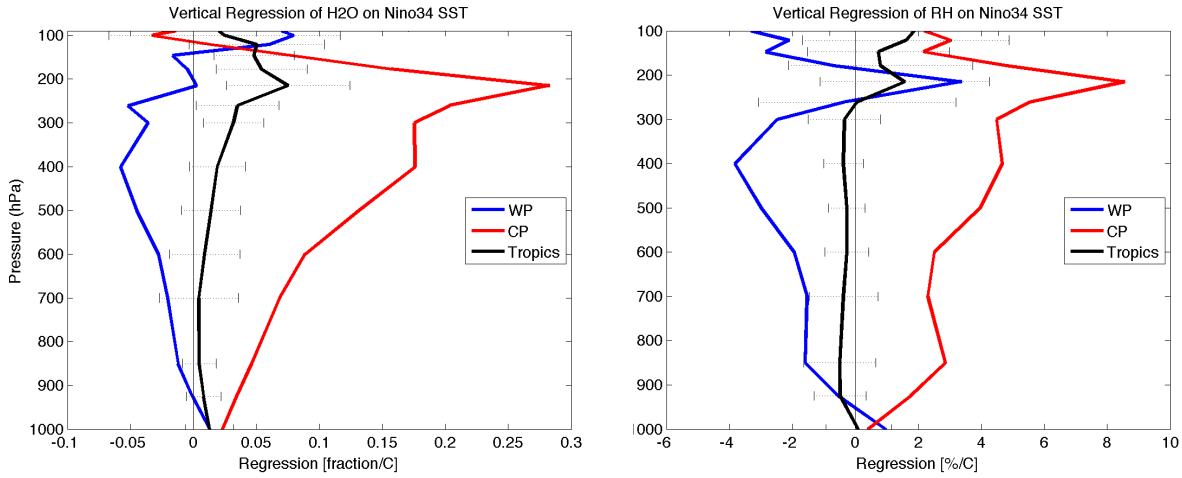

Figure 4.8. Regression of the fractional change in water vapor (left panel) with the error bars (σ) centered at zero and relative humidity anomalies (right panel) over tropics (black line: 30°S - 30°N), western Pacific (blue line: 10°S -10°N and 100 - 150°E) and over central Pacific (read line: 10°S -10°N and 160 - 200°E).

Chapter 5

Conclusions and Future Works

5.1. Summary of results

This thesis explores A-Train observations (e.g., CloudSat, AIRS, and MLS) and ISCCP CT data to seek new insights into tropical overshooting convection (OSC), convective outflow, and water vapor variations. Specifically, three subjects are identified for detailed studies: 1) observational determination of level of neutral buoyancy (LNB) for deep convection and comparison with the prediction based on the parcel theory, 2) characters and life stage view of tropical overshooting convection (OSC), and 3) vertical distribution of water vapor and clouds during two different types of El Niños: East Pacific –and Central Pacific. Here, we summarize the main findings.

5.1.1. Observational determination of LNB from CloudSat

In Chapter 2, we reconsidered the validity and applicability of LNB_sounding by introducing a new method for finding the LNB_observation directly from CloudSat. A near-global survey of LNB_observations (LNB_CTH, LNB_CHB, and LNB_maxMass) for tropical deep convection was made and comparison with the corresponding LNB_sounding is conducted. There are four primary findings. First, LNB_sounding can be used to identify the highest detrainment level (upper bound for convective detrainment), yet the correlation between LNB_sounding and LNB_CTH is poor (0.29). As a result, LNB_sounding itself cannot predict actual LNB precisely. Second, LNB_sounding is more than 3 km higher than the maximum mass detrainment level (LNB_maxMass). LNB_sounding clearly overestimates the level of convective

mass transport. Third, all three forms of LNB_observation are higher over land than over the ocean. On the other hand, there is not much land-ocean variation in LNB_sounding. Consequently, differences between LNB_observation and LNB_sounding are smaller over land than ocean because continental deep convection manages to detrain mass at a higher level, closer to the LNB derived from the sounding. Our results also show that oceanic convective systems are larger than continental convective systems, while the convective cores embedded in deep convection are larger over land than over ocean. Finally, we evaluated convective entrainment rate using an entraining plume model. The mean bulk entrainment rate for LNB_CTH, LNB_maxMass, and LNB_CBH are 3%/km, 6%/km, and 10%/km, respectively. Those values are slightly smaller over land than over ocean.

5.1.2. Tropical overshooting convection from a satellite perspective

Chapter 3 focuses on using CloudSat data together with the ISCCP CT database to characterize tropical OSC and the cloud systems in which they are embedded. OSC features are selected by the following assumptions: 1) CTH $\geq$ 10000 m; 2) CBH $\leq$ 2000 m; 3) continuity in radar echo from CBH to CTH; 4) CPR Cloud Mask $\geq$ 20; and 5) CTH > LNB + 500m. The occurrence frequency of OSC is approximately 0.46% over the entire tropics. Our results show that approximately 21.3% of tropical DC has overshooting tops, which is generally consistent with statistics obtained in previous studies using IR measurements. Continental convection has a slightly higher frequency of overshooting tops relative to oceanic convection.

We analyze various parameters to characterize cloud vertical extent (CTH), convective intensity (ETH, OSD and CTETD), and convective environment (LNB). Our results show that the vertical development of OSC tends to scale with LNB and that the convective strength and

cloud depth are closely related. Our results confirm that independent proxies of convective strength agree with each other fairly well, showing that tropical Africa has the strongest convective intensity among all the regions, which is consistent with our general understanding of tropical deep convection.

The distribution of maximum radius size (max R) and lifetime are similar over ocean and land, while the differences in the distribution of minimum brightness temperature (min Tb) between oceanic and continental convection are more significant: continental convection tends to have colder min Tb than oceanic convection. The normalized occurrence frequencies of OSC embedded in three stages of convection (defined as the total number of OSC embedded in each stage divided by the lifetime duration of each stage) reveals that OSC occurs predominantly during the growing stage of the CSs (~ 66.2% of all overshooting cases). The mature stage comes second (~33.4%). Only a very few cases (~ 0.4%) are found during the dissipating stage. Our proxies for convective strength from CloudSat also show that the vertical intensity of OSC at the growing stage is generally stronger than that at the mature stage. We further applied this analysis for convection over land versus over ocean and for local noon (1:30 p.m.) versus local midnight (1:30 a.m.). Result show that there is little variation between noontime and midnight over ocean but large variations over land. OSC at the mature stage is more abundant over land during noontime, which is due to the strong diurnal forcing from surface heating (intense heating during noon and nocturnal cooling).

5.1.3. Vertical distribution of water vapor during EP- and CP-El Niños

Water vapor is an important component of the atmosphere that interacts closely with convection. The water vapor distributions during the two different El Niño events, an EP-El Niño

(2006-7 DJF) and a CP-El Niño (2009-10 DJF), were analyzed together with CFr and CWC. These results were then compared with GFDL AM2.1 model simulations of water vapor and clouds to evaluate how realistically the model simulates the two El Niño events. Our results show that both El Niños strongly hydrate the upper troposphere around 200 hPa and slightly dry out the mid-troposphere around 700 hPa in terms of the tropical mean. Changes in the thermodynamic structure of the atmosphere play a key role in the water vapor response to the 2006–07 El Niño, whereas the water vapor response to the 2009–10 El Niño is forced by both thermodynamic and large-scale circulation changes. Moreover, regression analysis of water vapor anomalies onto the Niño-3.4 SST shows clear upper tropospheric amplification (i.e., strong peak in moistening around 200 hPa in response to the SST warming) of the fractional water vapor change to El Niño. The fractional increase rate of water vapor with Niño-3.4 SST exceeds the Clausius-Clapeyron value of 0.07/C, which has the highest value of 0.28/C around 200 hPa over the central Pacific where the largest convective anomalies are observed. Furthermore, the GFDL AM2.1 model simulates the general patterns of water vapor response to the ENSO SST forcing on the zonal and meridional plane.

However, water vapor distributions sorted by large-scale regimes are very different compared to observations during the 2009–10 El Niño. This discrepancy is found to be mainly due to simulation errors over the Indian Ocean. GFDL AM2.1 also does not reproduce realistic convective processes, which fail to simulate a strong moistening effect at 200 hPa where convective detrainment preferably occurs.

5.2. Limitations

Although we made some improvements on the current methods that were used to estimate convective mass detrainment level, intensity, and life stage of tropical deep convection, there are a few limitations that are worth mentioning.

First, we discussed the uncertainty of the sounding-based estimation of LNB in comparison with the observation-based counterpart. However, it should be noted that the observation-based method to estimate LNB, as shown in Chapter 2, requires "perfect" overpass by CloudSat to capture both convective core and mature anvils. Such cases are rare (only 4,008 cases found for 2.5 years of CloudSat data) due to narrow swath of CloudSat CPR. So, statistics may not be as robust in certain regions where such "perfect" deep convection is scarce. More data are needed to ensure the statistical significance. Fortunately, CloudSat mission has been extended to 2017 and a follow-on mission, EarthCARE is scheduled to be launched in 2016. So when more data become available, we will revisit the subject as investigated in Chapter 2.

Second, as shown in Chapter 3, data from CloudSat and collocated ECMWF analyses provide a means for selecting overshooting features. Also, we track the evolution of overshooting convection and determine its life cycle through joint analysis of CloudSat and the ISCCP CT database (the latter is based on geostationary satellite data). However, due to the fact that the A-Train constellation has ~1:30 a.m./p.m. equatorial crossing time, it is impossible to observe all OSC all the time and everywhere. One consequence is that we were unable to fully capture the diurnal variations in tropical deep convection. This limitation is more serious over land than ocean because the diurnal cycle of deep convection is the most pronounced over land. Usually, continental deep convection has a peak during late afternoon (e.g., Soden, 2000; Liu and Zipser, 2005). To understand how this may affect our statistics, we conduct a simple analysis

of the ISCCP CT data by plotting the diurnal variation in occurrence frequency of cold plumes embedded in CSs whose cloud tops have min TB_{IR} <245K, min TB_{IR} <220K, and min TB_{IR} <190K (based on data from Sep 2006-June 2008). They correspond roughly to the cloud-top height of 9 km, 12.5 km, and 17 km, respectively. Analysis is done for the whole tropics (30S-30N) and land and ocean separately (Figure 5.1). Figure 5.1 clearly shows that the diurnal cycle of OSC (e.g., min TB_{IR} <220K and min TB_{IR} <190K) is stronger over land than over ocean. The colder (or higher) the OSC, the larger the amplitude of the diurnal cycle (e.g., the group corresponding to min TB_{IR} <190K has the largest diurnal amplitude). We also notice a semi-diurnal cycle over land (peaks are early morning and late afternoon), but this subject is beyond the scope of our current work. Therefore, although our results in Chapter 3 show certain aspects of the diurnal variations of OSC over land (e.g., the OSC at the mature stages are more abundant over land during noontime), statistics should be considered tentative and should be revisited when the whole diurnal cycle is sampled. Nevertheless, it should be noted that CloudSat observes the internal vertical structure and intensity of OSC – a dimension that was not observed from previous passive sensors. This new aspect should add to our collective knowledge of the property and behaviors of tropical OSC.

5.3. Future works

Through this thesis, we gained new insights into the climatology, intensity, and life stage of tropical OSC. Yet there are several aspects of the mechanisms of OSC that need further investigation. Lifetimes for regular CSs are usually between 12 and 36 h (Futyan and Del Genio, 2007), whereas the lifetime of a hurricane can exceed a week. A previous study using IR data has found a "disproportionately" large amount of penetrative deep convection in tropical cyclones

(Romps and Kuang, 2009). Therefore, a sizable portion of OSC could be embedded in the hurricane eyewall transporting energy upward constantly throughout its lifetime. It is of interest to study the OSC that is embedded in hurricanes by comparing the CloudSat Tropical Cyclone data set (http://reef.atmos.colostate.edu/~natalie/tc) with the analysis presented in this paper. In parallel with the OSC study, we managed to evaluate the concept of LNB, which will connect deep convective outflow to UT/LS trace gases. We also document the vertical distribution of clouds and water vapor associated with ENSO events that motivates us to further investigate the influence of OSC on UT/LS water vapor and temperature using MLS and AIRS. Another interesting direction for future research would be to verify how much energy is transported by OSC from the boundary layer to the UT/LS using reanalysis datasets from, for example, the National Centers for Environmental Prediction and the National Center for Atmospheric Research (NCEP/NCAR reanalysis) or from ECMWF (ERA-40 reanalysis). Such an evaluation would constitute an important new contribution to understanding the roles of OSC in maintaining the energy balance of the tropics.

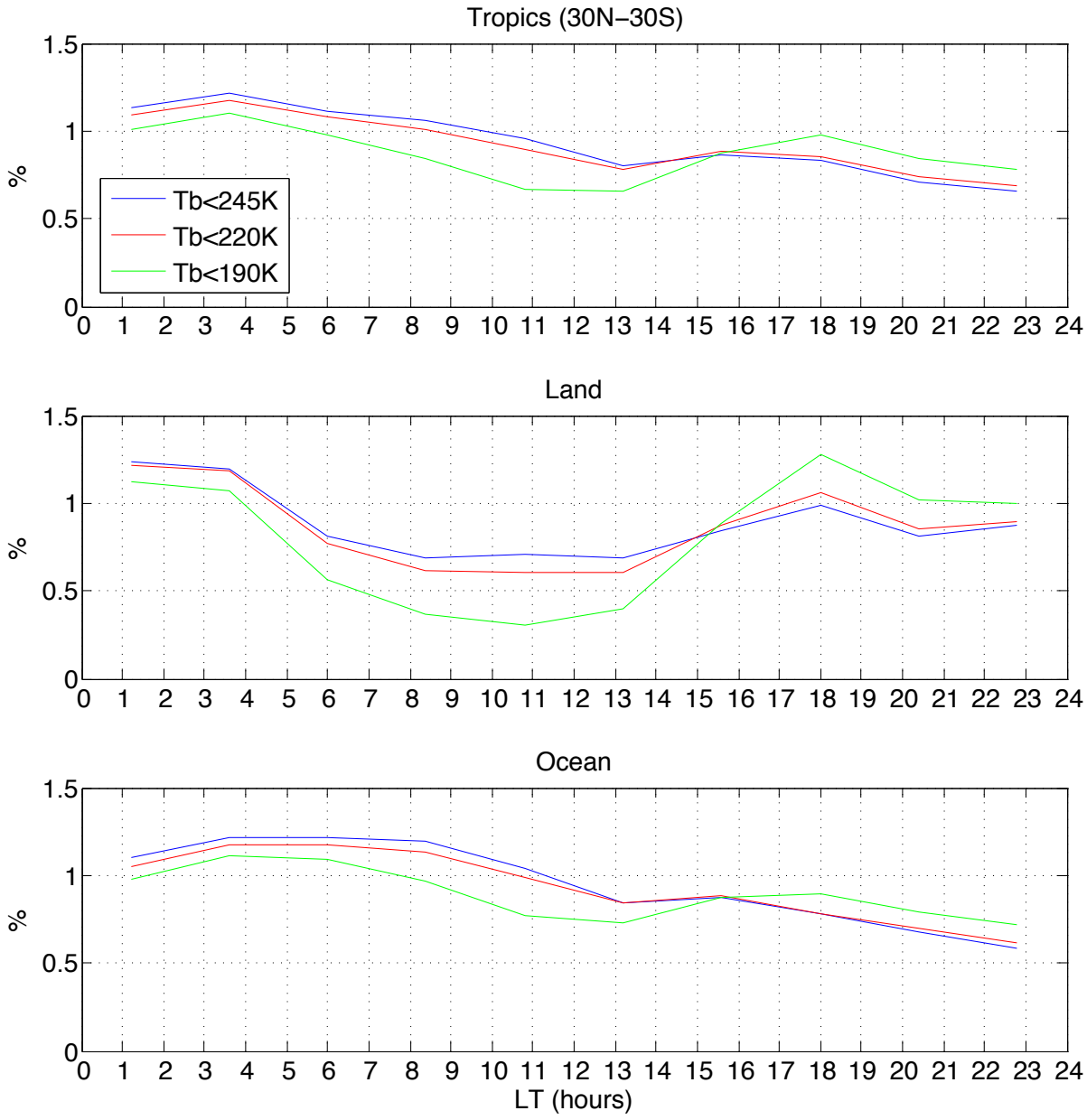

Figure 5.1. Diurnal variations in occurrence frequency of cold plumes embedded in CSs based on ISCCP CT data. Three thresholds are used to represent different height level deep convection: minimum cloud top temperature min TB_{IR} <245K, min TB_{IR} <220K, and min TB_{IR} <190K. The three panels from top to bottom are for all tropics (30S-30N), land, and ocean, respectively.

Bibliography

Alcala, C. M., and A. E. Dessler (2002), Observations of deep convection in the tropics using the Tropical Rainfall Measuring Mission (TRMM) precipitation radar, *Journal of Geophysical Research*, *107*, D24.

Allan R. P., A. S., and M. A., Ringer (2002), Influence of Dynamics on the Changes in Tropical Cloud Radiative Forcing during the 1998 El Niño, *J. Climate*, *15*, 1979-1986.

Anderson, L. J., et al. (2004), The New GFDL Global Atmosphere and Land Model AM2 LM2: Evaluation with Prescribed SST Simulations, *J. Climate*, *17*, 4641–4673.

Annamalai, H., K. Hamilton, and K.R. Sperber (2007), South Asian Summer Monsoon and its relationship with ENSO in the IPCC AR4 simulations, *J. Climate*, *20*, 1071–1092.

Arakawa, A., and W. H. Schubert (1974), Interaction of a cumulus cloud ensemble with the large scale environment. Part I, *J. Atmos. Sci*, *31*, 674-701.

Ashok, K., S. K. Behera, S. A. Rao, H. Weng, and T. Yamagata (2007), El Niño Modoki and its possible teleconnection, *Journal of Geophysical Research*, *112*, C11007.

Aumann, H. H., et al. (2003), AIRS/AMSU/HSB on the aqua mission: Design, science objectives, data products, and processing systems, IEEE Trans, *Geosci. Remote Sens.*, *41*, 253 – 264.

Bacmeister, J. T., and G. L. Stephens (2011), Spatial statistics of likely convective clouds in CloudSat data, *Journal of Geophysical Research*, *116*(D04104).

Bedka, K., J. Brunner, R. Dworak, W. Feltz, J. Otkin, and T. Greenwald (2010), Objective Satellite-Based Detection of Overshooting Tops Using Infrared Window Channel Brightness Temperature Gradients, *Journal of Applied Meteorology and Climatology*, *49*(2), 181-202.

Bedka, K. M., R. Dworak, J. Brunner, and W. Feltz (2012), Validation of Satellite-Based Objective Overshooting Cloud-Top Detection Methods UsingCloudSatCloud Profiling Radar Observations, *Journal of Applied Meteorology and Climatology*, *51*(10), 1811-1822.

Betts, A. K. (1990), Greenhouse warming and the tropical water budget, *Bull. Amer. Meteor. Soc*, *71*, 1464-1465.

Bjerknes, J. (1938), Saturated-adiabatic ascent of air through dry-adiabatically descending environment., *Q. J. R. Meteorol. Soc.*, *64*, 325 – 330.

Bony, S., J. L. Dufresne, H. Le Treut, J. J. Morcrette, and C. Senior (2004), On dynamic and thermodynamic components of cloud changes, *Climate Dynamics*, *22*(2-3), 71-86.

Cess, R. D., M. Zhang, B. A. Wielicki, D. F. Young, X. Zhou, and Y. Nikitenko (2001), The influence of the 1998 El Niño upon cloud radiative forcing over the Pacific warm pool, *J. Climate*, *14*, 2129–2137.

Cetrone, J., and R. A. Houze (2009), Anvil clouds of tropical mesoscale convective systems in monsoon regions, *Quarterly Journal of the Royal Meteorological Society*, *135*(639), 305-317.

Chahine, M. T., et al. (2006), AIRS: Improving Weather Forecasting and Providing New Data on Greenhouse Gases, *Bulletin of the American Meteorological Society*, *87*(7), 911-926.

Chuang, H., X. Huang, and K. Minschwaner (2010), Interannual variations of tropical upper tropospheric humidity and tropical rainy-region SST: Comparisons between models, reanalyses, and observations, *Journal of Geophysical Research*, *115*, D21125.

Corti, T., et al. (2008), Unprecedented evidence for deep convection hydrating the tropical stratosphere, *Geophys. Res. Lett.*, *35*, L10810.

Danielsen, E. F. (1985), A dehydration mechanism for the stratosphere, *Geophys. Res. Lett.*, *9*, 605-608.

Danielsen, E. F. (1993), In situ evidence of rapid, vertical, irreversible transport of lower tropospheric air into the lower stratosphere by convective cloud turrets and by large scale up welling in tropical cyclones, *J. Geophys. Res.*, *98*, 8665–8681.

Delworth, T. L., and Coauthors (2006), GFDL's CM2 Global Coupled Climate Models. Part I: Formulation and Simulation Characteristics, *J. Climate*, *19*, 643–674.

Du, Y., S.-P. Xie, G. Huang, and K. Hu (2009), Role of air-sea interaction in the long persistence of El Nino-induced North Indian Ocean warming, *J. Climate*, *22*, 2023-2038.

Emanuel, K. A. (1994), Atmospheric convection, *Oxford University Press*, 580.

Fierro, A. O., Joanne Simpson, Margaret A. LeMone, Jerry M. Straka, Bradley F. Smull (2009), On How Hot Towers Fuel the Hadley Cell: An Observational and Modeling Study of Line-Organized Convection in the Equatorial Trough from TOGA COARE, *J. Atmos. Sci*, *66*, 2730-2746.

Fueglistaler, S., A. E. Dessler, T. J. Dunkerton, I. Folkins, Q. Fu, and P. W. Mote (2009), Tropical tropopause layer, *Rev.Geophys. Res. Lett*, *47*, RG1004.

Futyan, J. M., and Del Genio, A. D. (2007), Deep Convective System Evolution over Africa and the Tropical Atlantic, *J Climate*, *20*, 5041-5060.

Gettelman, A., and P. M. de F. Forster (2002), A climatology of the tropical tropopause layer, J. Meteorol, *Soc. Jpn*, *80*(4B), 911 – 924.

Gettelman, A., M. L. Salby, and F. Sassi (2002), The distribution and influence of convection in the tropical tropopause region, *J. Geophys. Res*, *107*, 4080.

Hassim, M. E. E., and T. P. Lane (2010), A model study on the influence of overshooting convection on TTL water vapour, *Atmos. Chem. Phys.*, *10*(20), 9833-9849.

Holton, J. R. a. G., A (2001), Horizontal transport and the dehydration of the stratosphere, *Geophys. Res. Lett.*, *28*, 2799-2802.

Hong, G., G. Heygster, J. Miao, and K. Kunzi (2005), Detection of tropical deep convective clouds from AMSU-B water vapor channels measurements, *J. Geophys. Res.*, *110*, D05205.

Houze, R. A. (1997), Stratiform Precipitation in Regions of Convection: A Meteorological Paradox?, *Bull. Amer. Meteor. Soc.*, *78*, 2179–2196.

Houze, R. A. (2003), From Hot Towers to TRMM: Joanne Simpson and Advances in Tropical Convection Research, *Meteorological Monographs*, *29*, 37-37.

Im, E., S. L. Durden, and C. Wu (2006), Cloud profiling radar for the CloudSat mission. IEEE Trans, *Aerosp. Electron. Syst*, *20*, 15–18.

Iwasaki, S., T. Shibata, J. Nakamoto, H. Okamoto, H. Ishimoto, and H. Kubota (2010), Characteristics of deep convection measured by using the A-Train constellation, *J. Geophys. Res.*, *115*, D06207.

Iwasaki, S., T. Shibata, H. Okamoto, H. Ishimoto, and H. Kubota (2012), Mixtures of stratospheric and overshooting air measured using A-Train sensors, *Geophys. Res.*, *117*, D12207.

Jensen, E. J., A. S. Ackerman, and J. A. Smith (2007), Can overshooting convection dehydrate the tropical tropopause layer?, *Geophys. Res.*, *112*, D11209.

Jiang, J. H., H. Su, S. Pawson, H.C. Liu, W. Read, J.W. Waters, M. Santee, D.L. Wu, M. Schwartz, N. Livesey, A. Lambert, R. Fuller, and J.N. Lee (2010), Five-year (2004-2009) Observations of Upper Tropospheric Water Vapor and Cloud Ice from MLS and Comparisons with GEOS-5 analyses, *J. Geophys. Res.*, *115*, D15103.

Jiang, J. H., et al. (2012), Evaluation of cloud and water vapor simulations in CMIP5 climate models using NASA "A-Train" satellite observations, *J. Geophys. Res*, *117*, D14105.

Kao, H. Y., and J.-Y. Yu (2009), Contrasting Eastern-Pacific and Central-Pacific Types of ENSO, *J. Climate*, *22*(3), 615-632.

Khaykin, S., Pommereau, J.-P., Korshunov, L., Yushkov, V.,, J. Nielsen, Larsen, N., Christensen, T., Garnier, A., Lukyanov,, and a. W. A., E (2009), Hydration of the lower stratosphere by ice crystal geysers over land convective system, *Atmos. Chem. Phys.*, *9*, 2275–2287.

Kim, D., Y.-S. Jang, D.-H. Kim, Y.-H. Kim, M. Watanabe, F.-F. Jin, and J.-S. Kug (2011), El Niño–Southern Oscillation sensitivity to cumulus entrainment in a coupled general circulation model, *J. Geophys. Res.*, *116*, D22112.

Kim, H., P. J. Webster, and J. A. Curry (2009), Impact of Shifting Patterns of Pacific Ocean Warming on North Atlantic Tropical Cyclones, *Science*, *325*, 77.

Klein, S. A., B.J. Soden and N.-C. Lau (1999), Remote sea surface temperature variations during ENSO: Evidence for a tropical atmospheric bridge, *J. Climate*, *12*, 917-932.

Kuang, Z. M., and C. S. Bretherton (2004), Convective Influence on the Heat Balance of the Tropical Tropopause Layer: A Cloud-Resolving Model Study, *J. Atmos. Sci*, *61*, 2919- 2927.

Kug, J.-S., Jin, F.-F. and An, S.-I. (2009), Two Types of El Niño Events: Cold Tongue El Niño and Warm Pool El Niño, *J. Climate*, *22*(6), 1499-1515.

Kumar, A., and M. P. Hoerling (1998), Specification of regional sea surface temperatures in atmospheric general circulation model simulations, *J. Geophys. Res*, *103*, 8901–8907.

Küpper, C., J. Thuburn, G. C. Craig, and T. Birner (2004), Mass and water transport into the tropical stratosphere: A cloud-resolving simulation, *J. Geophys. Res*, *109*, D10111.

L'Ecuyer, T. S., and J.H. Jiang (2010), Touring the atmosphere aboard the A-Train, *Physics Today 63*(7), 36-41.

Latif, M., Kleeman, R. and Eckert, C (1997), Greenhouse warming, decadal variability, or El Niño? An attempt to understand the anomalous 1990s, *J. Climate*, *10*, 2221–2239.

Lau, N.-C., Ants Leetmaa, Mary Jo Nath (2006), Attribution of Atmospheric Variations in the 1997–2003 Period to SST Anomalies in the Pacific and Indian Ocean Basins, *J. Climate*, *19*, 3607–3628.

Le Marshall, J., Jung, J., Derber, J., Treadon, R., Lord, S.J., Goldberg, M., Wolf, W., Liu, H.C., Joiner, J., Woolen, J., Todling, R., Gelaro, R. (2005), Impact of Atmospheric InfraRed Sounder observations on weather forecasts. EOS, *Trans. Amer. Geophys. Union*, *86*, 109,115,116.

Li, W., and C. Schumacher (2010), Thick Anvils as Viewed by the TRMM Precipitation Radar, *J. Climate*, *24*, 1718-1735.

Liu, C., and E. J. Zipser (2005), Global distribution of convection penetrating the tropical tropopause, *J. Geophys. Res*, *110*, D23104.
Liu, C., E. J. Zipser, and S. W. Nesbitt (2007), Global distribution of tropical deep convection: Different perspectives from TRMM infrared and radar data, *J. Climate*, *20*, 489–503.

Liu, C., and E. J. Zipser (2008), Diurnal cycles of precipitation, clouds, and lightning in the tropics from 9 years of TRMM observations, *Geophys. Res. Lett*, *35*, L04819.

Livesey, N. J., W. V. Snyder, W. G. Read, and P. A. Wagner (2006), Retrieval algorithms for the EOS Microwave Limb Sounder (MLS) instrument, IEEE Trans, *Geosci. Remote Sens.*, *44*(5), 1144 – 1155.

Livesey, N. J., William G. Read, Lucien Froidevaux, Alyn Lambert, Gloria L. Manney,, M. L. S. Hugh C. Pumphrey, Michael J. Schwartz, Shuhui Wang, Richard E. Cof eld,, R. A. F. David T. Cuddy, Robert F. Jarnot, Jonathan H. Jiang, Brian W. Knosp,, and P. A. W. Paul C. Stek, and Dong L. Wu. (2011), Earth Observing System (EOS) Aura Microwave Limb Sounder (MLS) Version 3.3 Level 2 data quality and description document, *JPL D-33509, Jet Propul. Lab., Pasadena, Calif*(available at http://mls.jpl.nasa.gov/data/datadocs.php).

Lucas, C., M. A. LeMone, and E. J. Zipser (1994), Vertical velocity in oceanic convection off tropical Australia, *J. Atmos. Sci*, *51*, 3183–3193.

Luo, Y., R. Zhang, W. Qian, Z. Luo, and X. Hu (2011), Intercomparison of Deep Convection over the Tibetan Plateau–Asian Monsoon Region and Subtropical North America in Boreal Summer UsingCloudSat/CALIPSO Data, *Journal of Climate*, *24*(8), 2164-2177.

Luo, Z., G. Y. Liu, and G. L. Stephens, G. L. (2008), CloudSat adding new insight into tropical penetrating convection, *Geophys. Res. Lett*, *35*, L19819.

Luo, Z., G. Y. Liu, G. L. Stephens, and R. H. Johnson (2009), Terminal versus transient cumulus congestus: A CloudSat perspective, *Geophys. Res. Lett*, *36*, L05808.

Luo, Z. J., G. Y. Liu, and G. L. Stephens (2010), Use of A-Train data to estimate convective buoyancy and entrainment rate, *Geophys. Res. Lett*, *37*, L09804.

Luo, Z. J., D. Kley, R. H. Johnson, G. Y. Liu, S. Nawrath, and H. G. J. Smit (2012), Influence of Sea Surface Temperature on Humidity and Temperature in the Outflow of Tropical Deep Convection, *Journal of Climate*, *25*(4), 1340-1348.

Machado, L. A. T., W. B. Rossow (1993), Structural Characteristics and Radiative Properties of Tropical Cloud Clusters, *Mon. Wea. Rev*, *121*, 3234–3260.

Machado, L. A. T., W. B. Rossow, R. L. Guedes, and A. W. Walker (1998), Life cycle variations of mesoscale convective systems over the Americas, *Mon. Wea. Rev*, *126*, 1630–1654.

Manabe, S. and Wetherald, R. (1967): Thermal equilibrium of the atmosphere with a given distribution of relative humidity. *J. of Atmos. Sci., 24*, 241–259.

Manzato, A., Morgan Jr., G.M (2003), Evaluation of the sounding instability with the lifted parcel theory, *Atmos. Res.*, *67–68*, 455–573.

Mullendore, G. L., A. J. Homann, K. Bevers, and C. Schumacher (2009), Radar reflectivity as a proxy for convective mass transport, *Journal of Geophysical Research*, *114*, D16103.

Olsen, E. T., S. Granger, E. Manning, and J. Blaisdell (2007), AIRS/AMSU/HSB Version 5 Level 3 Quick Start, report, 25 pp, *Jet Propul. Lab., Pasadena, Calif*(Available at http://disc.sci.gsfc.nasa.gov/AIRS/documentation/v5_docs/AIRS_V5_Release_User_Docs/V5_L3_QuickStart.pdf.).

Ramanathan, V., and W. Collins (1991), Thermodynamic regulation of ocean warming by cirrus clouds deduced from observations of the 1987 El Niño, *Nature*, *351*, 27–32.

Read, W. G., et al (2007), Aura Microwave Limb Sounder upper tropospheric and lower stratospheric H2O and relative humidity with respect to ice validation, *J. Geophys. Res*, *112*.

Richter, I., and S.-P. Xie (2008), Muted precipitation increase in global warming simulations: A surface evaporation perspective, *J. Geophys. Res*, *113*, D24118.

Riehl, H., and J. S. Malkus (1958), On the heat balance in the equatorial trough zone, *Geophysica*, *6*, 503–538.

Riehl, H., and Simpson, J. S (1979), On the heat balance in the equatorial trough zone, revisited, *Contrib. Atmos. Phys*, *52*, 287–305.

Riley, E. M., and B. E. Mapes (2009), Unexpected peak near -15°C in CloudSat echo top climatology, *Geophys. Res. Lett*, *36*, L09819.

Romps, D. M., and Z. Kuang (2009), Overshooting convection in tropical cyclones, *Geophys. Res. Lett*, *36*(9), L09804.

Rossow, W. B., and C. Pearl (2007), 22-Year survey of tropical convection penetrating into the lower stratosphere, *Geophys. Res. Lett*, *34*, L04803.

Sherwood, C. S., T. Horinouchi and H. A. Zeleznik (2003), Convective impact on temperatures observed near the tropical tropopause, *J. Atmos. Sci*, *60*, 1847 – 1856.

Sherwood, S. C., and A. E. Dessler (2000), On the control of stratospheric humidity, *Geophys. Res. Lett*, *27*, 2513–2516.

Soden, B. J., and R. Fu (1995), A satellite analysis of deep convection, upper tropospheric humidity, and the greenhouse effect, *J. Climate*, *8*, 2333–2351.

Soden, B. J. (2000), The diurnal cycle of convection, clouds, and water vapor in the tropical upper troposphere, *Geophys. Res. Lett.*, *27*, 2173-2176.

Stephens, G. L., D.G. Vane, R.J. Boain, G.G. Mace, K. Sassen, Z. Wang, A.J. Illingworth, E.J. O'Connor, W.B. Rossow, S.L. Durden, S.D. Miller, R.T. Austin, A. Benedetti, C. Mitrescu, and

CloudSat Science Team (2002), The CloudSat mission and the A-Train: A new dimension of space-based observations of clouds and precipitation, *Bull. Amer. Meteorol. Soc*, *83*, 1771-1790.

Stephens, G. L., et al (2008), CloudSat mission: Performance and early science after the first year of operation, *J. Geophys. Res*, *113*, D00A18.

Su, H., W.G. Read, J.H. Jiang, J.W. Waters, D.L. Wu, and E.J. Fetzer (2006), Enhanced positive water vapor feedback associated with tropical deep convection: New evidence from Aura MLS, *Geophys. Res. Lett*, *33*, L05709.

Su, H., J.H. Jiang, J. Teixeira, A. Gettelman, X. Huang, G. Stephens, D. Vane, and V.S. Perun (2011), Comparison of Regime-Sorted Tropical Cloud Profiles Observed by CloudSat with GEOS5 Analyses and Two General Circulation Model Simulations, *J. Geophys. Res*, *116*, D0910.

Su, H., and J.H. Jiang (2013), Tropical Clouds and Circulation Changes During the 2006-07 and 2009-10 El Niños, *J. Climate*, *26*, 399-413.

Sun, D.-Z., Richard S. Lindzen (1993), Distribution of Tropical Tropospheric Water Vapor, *J. Atmos. Sci*, *50*, 1643–1660.

Sun-Mack, S., et al (2007), Integrated cloud-aerosol-radiation product using CERES, MODIS, CALISPO, and CloudSat data, *Proc. SPIE Int. Soc. Opt. Eng*, *6745*, 1 – 11.

Takahashi, H., and Z. Luo (2012), Where is the level of neutral buoyancy for deep convection?, *Geophys. Res. Lett*, *39*(15).

Tao, W.-K., J. Halverson, M. LeMone, R. Adler, M. Garstang, R. Houze, Jr., R. Pielke, Sr., and W. Woodley (2003), The research of Dr. Joanne Simpson: Fifty years investigating hurricanes, tropical clouds, and cloud systems, *Meteorological Monographs*, *29*, 1-16.

Tian, B., E.J. Fetzer, B.H. Kahn, J. Teixeira, E. Manning, T. Hearty (2013), Evaluating CMIP5 models using AIRS tropospheric air temperature and specific humidity climatology, *J. Geosphys. Res*., 118, doi:10.1029/2012JD018607.

Waters, J. W., et al (2006), The Earth observing system microwave limb sounder (EOSMLS) on the Aura satellite, IEEE Trans, *Geosci. Remote Sens.*, *44*(5), 1075 – 1092.

Weng, H., K. Ashok, S. K. Behera, S. A. Rao, and T. Yamagata (2007), Impacts of recent El Niño Modoki on dry/wet conditions in the Pacific rim during boreal summer, *Clim. Dyn*, *29*, 113-129.

Weng, H., Behera, S. K. and Yamagata (2009), Anomalous winter climate conditions in the Pacific Rim during recent El Niño Modoki and El Niño events, *Clim. Dyn*, *32*, 663–674.

Winker, D. M., J. R. Pelon, and M. P. McCormick (2003), The CALIPSO mission: Spaceborne lidar for observation of aerosols and clouds, *Proc. of SPIE*, *4893*, 1–11.

Yuan, J., and R.A. Houze. Jr (2010), Global Variability of Mesoscale Convective System Anvil Structure from A-Train Satellite Data, *J. Climate*, *23*, 5864-5888.
Yuan, J., R. A. Houze. Jr, and A. J. Heymsfield (2011), Vertical Structures of Anvil Clouds of Tropical Mesoscale Convective Systems Observed by CloudSat, *J. Atmos. Sci*, *68*, 1653–1674.

Zhang, M. H., R. D. Cess, and S. C. Xie (1996), Relationship between Cloud Radiative Forcing and Sea Surface Temperatures over the Entire Tropical Oceans, *J. Climate*, *9*, 1374–1384.

Zipser, E. J. (2003), Some Views On "Hot Towers" after 50 Years of Tropical Field Programs and Two Years of TRMM Data, *Meteorological Monographs*, *29*(51), 49–58.

Zipser, E. J., Chuntao Liu, Daniel J. Cecil, Stephen W. Nesbitt, David P. Yorty (2006), Where are the most intense thunderstorms on Earth?, *Bull. Am. Meteorol. Soc*, *87*, 1057–1071.